Pre-print submitted version

Efficient wide-bandgap mixed-cation and mixed-halide perovskite solar cells by vacuum deposition

Lidón Gil-Escrig,[a] Chris Dreessen,[a] Francisco Palazon,[a] Zafer Hawash,[b] Ellen Moons,[b] Steve Albrecht,[c] Michele Sessolo,[a,*] and Henk J. Bolink[a]

[a]*Instituto de Ciencia Molecular, Universidad de Valencia, C/ Catedrático J. Beltrán 2, 46980, Paterna, Spain. E-mail:* michele.sessolo@uv.es

[b]*Department of Physics, Karlstad University, SE-65188 Karlstad, Sweden*

[c]*Young Investigator Group for Perovskite Tandem Solar Cells, Helmholtz-Center Berlin, Kekuléstrasse 5, 12489 Berlin, Germany*

ABSTRACT: Vacuum deposition methods are increasingly applied to the preparation of perovskite films and devices, in view of the possibility to prepare multilayer structures at low temperatures. Vacuum-deposited, wide-bandgap solar cells based on mixed cation and mixed anion perovskites have been scarcely reported, due to the challenges associated with the multiple-sources processing of perovskite thin-films. In this work, we describe a 4-sources vacuum deposition process to prepare wide-bandgap perovskites of the type $FA_{1-n}Cs_nPb(I_{1-x}Br_x)_3$ with tunable bandgap and controlled morphology, using FAI, CsI, PbI_2 and $PbBr_2$ as the precursors. The simultaneous sublimation of PbI_2 and $PbBr_2$ allows to decouple and control the relative Br/Cs content, resulting in homogeneous perovskite films with bandgap in the 1.7 eV-1.8 eV range and no detectable halide segregation. Solar cells based on 1.75 eV bandgap perovskites show efficiency up to 16.8% and promising stability, maintaining 90% of the initial efficiency after 2 weeks of operation.

Among emerging photovoltaic (PV) technologies, thin-film solar cells based on organic-inorganic (hybrid) lead halide perovskites (herein called perovskites) are by far the most widely investigated. The interest towards these materials is driven by the possibility to deposit high quality semiconducting films with simple and low energy-demanding processes.[1–6] This feature is a consequence of the high tolerance to defects,[7,8] conferring perovskites with low trap density and long carrier diffusion length.[9–

[14] As a result, the efficiency of single junction solar cells has grown considerably within only a decade of development,[15] with a record power conversion efficiency (PCE) now exceeding 25%.[16] An important property of perovskites is the possibility of readily tune their bandgap,[17–20] making them a suitable candidate for applications in single-junction as well as multijunction solar cells,[21–24] e.g. in combination with narrow-bandgap absorbers such as $Cu(In,Ga)Se_2$,[25–28] silicon,[29–35] or by using complementary perovskites.[36–42] Perovskite alloys of the type $ASn_{1-x}Pb_xI_3$ (where A is an organic or inorganic cation, or a mixture of them) have bandgaps in the 1.20-1.25 eV range for lead content $0.25 \leq x \leq 0.5$.[43,44] This requires perovskite compositions with wide bandgaps in the 1.75-1.85 eV range in order to aim at perovskite-perovskite tandem devices that can exceed the theoretical efficiency limit of single junction solar cells.[21–24] Perovskite films with wide bandgaps suitable for perovskite-perovskite tandems can be readily obtained by using mixed iodide/bromide formulations,[17] and mixed A-site cations are also employed to improve the photo- and thermal stability of the compounds.[45–47] The study of wide-bandgap perovskite materials and solar cells is a booming field of research, well summarized in recent reviews[23,48] and in research articles containing some of the best performing devices to date.[49–51] In comparison with narrower-bandgap materials,[52] wide-bandgap perovskite solar cells suffer from a larger open-circuit voltage (V_{oc}) deficit, i.e. the V_{oc} does not scale linearly with the bandgap as predicted by the Shockley-Queisser (SQ) limit. This deviation is due to non-radiative recombination in the perovskite bulk and at the interface with the transport layers.[51,53–55] For this reason, a large number of studies aimed at developing bulk and surface passivation strategies, as well as to identify suitable transport layers and contacts.[56–60]

The vast majority of studies on wide-bandgap perovskite solar cells relied on solution-processed perovskite thin-films. Vacuum deposition is an alternative method with superior control over the film thickness and composition; it is compatible with large areas and eliminates the processing concerns related with the use of solvents.[61–63] This is especially relevant for the fabrication of complex multilayer architectures, necessary for tandem solar cells.[37,64] Moreover, vacuum deposition allows the deposition of pinhole-free, uniform and smooth films.[65–68] Early reports on vacuum-deposited wide-bandgap perovskites used the simplest formulation, methylammonium lead iodide-bromide, $MAPb(I_{1-x}Br_x)_3$. We showed that these type of compounds with bandgap (E_g) up to 1.7 eV ($x \approx 0.2$), are stable even at high irradiance levels, and the corresponding perovskite solar cells exhibited PCE up to 15.9%.[69] When the amount of bromide is increased ($x \geq 0.3$), the perovskite demixes into iodide- and bromide-rich phases in a process known as “halide segregation”,[45,70,71] which can be readily monitored from the red-shifted perovskite photoluminescence (PL) spectrum.[69,72] The iodide-rich, narrow-bandgap regions can reduce the quasi-Fermi level splitting (QFLS) and hence the maximum attainable

V_{oc}. Phase-stable hybrid perovskite films with $E_g > 1.7$ eV require the use of mixed A-site cations such as cesium and formamidinium (Cs^+, FA^+).[45–47] We have previously demonstrated the deposition of the wide-bandgap $Cs_{0.5}FA_{0.4}MA_{0.1}Pb(I_{0.83}Br_{0.17})_3$ perovskite in a 4-sources co-sublimation process, from PbI_2, CsBr, formamidinium iodide (FAI) and methylammonium iodide (MAI) precursors.[73] CsBr was used simultaneously as the source of Cs^+ and Br^-, a strategy later adopted by others to reduce the number of deposition sources and precursors.[74,75] In those recent reports, $FA_{1-n}Cs_nPb(I_{1-x}Br_x)_3$ perovskites with intentionally low CsBr content ($x \leq 0.1$) were presented, targeting perovskites with bandgaps more suitable for single junction solar cells. In order to obtain a wide bandgap ($E_g > 1.7$ eV), substantial amount of Br^- needs to be incorporated, hence resulting in an equally large cesium concentration. The excess of cesium was found to cause an irregular morphology and substantial bulk recombination in the perovskite, limiting the device performance.[73]

In this work, we demonstrate an alternative 4-sources vacuum deposition process to prepare wide-bandgap perovskites of the type $FA_{1-n}Cs_nPb(I_{1-x}Br_x)_3$ with tunable bandgap and controlled morphology, using FAI, CsI, PbI_2 and $PbBr_2$ as the precursors. The simultaneous sublimation of the two lead halides allows to decouple and control the relative bromide/cesium content, resulting in homogeneous perovskite films with bandgap in the 1.7 eV-1.8 eV range and no detectable halide segregation. Solar cells based on 1.75 eV bandgap perovskites show PCE up to 16.8% and promising stability, maintaining 90% of the initial efficiency after 2 weeks of continuous operation in inert atmosphere.

The mixed-cation lead mixed-halide perovskites were deposited by simultaneous vacuum deposition of the precursors FAI, CsI, PbI_2 and $PbBr_2$. In order to calibrate the deposition rate of each material, the specific tooling factors were determined by individually subliming them and comparing the thickness displayed from the quartz crystal microbalance (QCM) with the one measured with a mechanical profilometer. Unlike MAI, which exhibits non-standard sublimation properties,[76] the FAI adhesion is rather independent on the chemical composition of the surface,[77] and hence the FAI deposition rate can be monitored with a dedicated QCM placed nearby the corresponding thermal source. The details of the experimental conditions are provided in the Supporting Information. We prepared four perovskite compositions with increasing Br^-/I^- and FA^+/Cs^+ ratios, with the aim to increase the bandgap while ensuring phase stability. After several variations, we found the following procedure to lead to the best performing perovskite compositions. The FAI and PbI_2 deposition rates were kept constant at 0.8 Å/s and 1 Å/s, respectively. The $PbBr_2$ deposition rate was varied from 0.07 to 0.22 Å/s, while the CsI rate was increased from 0.25 to 0.45 Å/s, to prevent halide segregation in

the bromide-rich formulations. The substrates were kept at room temperature (RT) during deposition and the films were not annealed and used as-deposited.

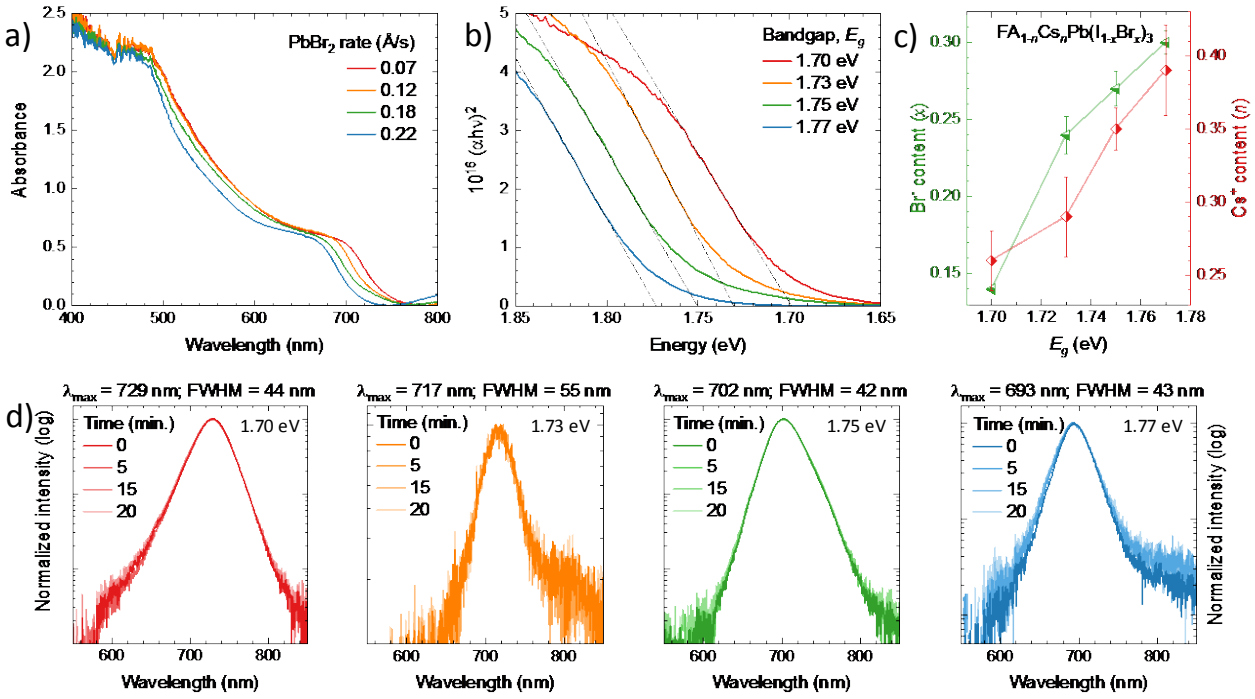

Figure 1. (a) Absorbance spectra of a series of $FA_{1-n}Cs_nPb(I_{1-x}Br_x)_3$ perovskite films obtained with increasing the $PbBr_2$ deposition rate and (b) corresponding Tauc plot and estimated bandgap energies (E_g). The film thickness is 500 nm for all samples. (c) Bulk bromide (left, green) and cesium (right, red) content in the perovskite films estimated by energy dispersive X-ray spectroscopy (EDS). Error bars are the standard deviation of measurements obtained from films of different deposition runs. (d) Normalized photoluminescence (PL) spectra of the same samples recorded over time (up to 20 minutes) under continuous illumination. The excitation source is a green laser (515 nm) with an irradiance of approximately 300 mW/cm^2.

The absorbance spectra of a series of 500 nm thick wide-band gap $FA_{1-n}Cs_nPb(I_{1-x}Br_x)_3$ perovskite films on glass substrates are reported in **Figure 1**a. All films show the expected perovskite absorption profile, with absorbance > 1 for wavelength below approximately 550 nm. With increasing $PbBr_2$ content (deposition rate), we observed the expected blue-shift of the absorption cutoff from approximately 740 nm to 690 nm, indicating that indeed bromide is incorporated into the perovskite structure. The corresponding Tauc plots (Figure 1b) allow to estimate the bandgap energy of the four perovskite compositions, with E_g increasing steadily from 1.70 eV to 1.77 eV. The bulk Cs^+ (n) and

Br^- (x) concentrations in the different $FA_{1-n}Cs_nPb(I_{1-x}Br_x)_3$ samples were estimated by energy dispersive X-ray spectroscopy (EDS). As highlighted in Figure 1c, bromide and cesium contents were found to be in the $0.14 \leq x \leq 0.30$ and $0.26 \leq n \leq 0.39$ ranges, respectively. The Cs^+ concentration was adjusted in order to stabilize the perovskite formulations against halide segregation, in particular when the bromide content is increased to obtain the wider-bandgap materials. In Figure S1, the photoluminescence (PL) spectra of perovskite films with 1.75 eV bandgap (x = 0.27) and varying amounts of Cs+ (n) are presented, showing that the perovskite is photo-stable for CsI deposition rates > 0.3 Å/s (n > 0.3, see discussion in the Supplementary Information and Figure S2). For this particular perovskite (E_g = 1.75 eV), we have performed further compositional analysis by using high resolution X-ray photoemission spectroscopy (HR-XPS) to measure the core levels of the perovskite elements. The collected spectra were consequently normalized, using the corresponding atomic sensitivity factors, to find the surface atomic composition.[78] The surface contents of bromide and cesium using HR-XPS was found to be x = 0.24, n = 0.40, respectively (Figure S3), only slightly different from the ones obtained by EDS. Taking into the difference in information depth into consideration for XPS[79] (only a few nanometers) and EDS[80] (several hundreds of nanometers), the results imply that there is no substantial compositional difference between the bulk and the surface of the perovskite films. In Figure 1d, the PL spectra of the entire series of stabilized perovskite films is reported. Spectra are collected over time under continuous wave laser illumination (515 nm), at an irradiance of approximately 300 mW/cm^2, corresponding to a 5 – 6 sun equivalent intensity. Note that after an initial drop of the PL intensity in the first 15-20 minutes, we found it to be stable for up to one hour of continuous measurement (Figure S4). Even with these harsh conditions, we did not observe any low energy PL components which would indicate halide segregation into iodide-rich regions. Note that a semi-logarithmic scale is used for all spectra in Figure 1d to highlight the persistence of a single PL component. The differences in linewidth are due to varying signal-to-noise ratios among the different samples, hence the full width at half maximum (FWHM) measured by Gaussian fit is reported for reference. We observed photoinduced halide segregation only when the bromide content x was increased to 0.4 (Figure S5), indicating that the perovskite formulation should be substantially modified in order to obtain phase-stable materials with high bromide content. We have also measured the PL spectra for a perovskite film on glass, exciting the sample both from the glass and from the perovskite side. As shown in Figure S6, the spectral shape and position is unaltered, suggesting that there are no obvious compositional changes through the cross-section of the film. The lower PL intensity observed when shining the laser directly on the perovskite film indicates a larger degree of non-radiative recombination at the perovskite surface. In order to estimate the reproducibility of the deposition process, we compared the PL spectra for films obtained from seven consecutive deposition

runs. As depicted in Figure S7, the bandgap variation for seven different batches of the perovskite with bandgap of 1.75 eV is of only 17 meV, demonstrating the good reproducibility of the vacuum deposition process.

The perovskite films were further analyzed by X-ray diffraction (XRD, Figure 2a). The XRD data can be fitted considering a single distorted perovskite phase in combination with a marginal contribution from PbI_2, which is mostly visible by its main peak around $2\theta = 12.8^{\circ}$. The perovskite phase considered here corresponds to the space group Pnma (orthorhombic system), which is the reported stable phase of $CsPbBr_3$ and $MAPbBr_3$ at room temperature (see Inorganic Crystal Structure Database, ICSD references #243735 and #158306). This can be considered a "lower-symmetry" derivative (hettotype) of the highest-symmetry cubic perovskite (aristotype; space group Pm-3m), where PbX_6 octahedra are slightly tilted (see scheme in Figure S8).[81] All samples show a clear preferential orientation along the b-axis (perpendicular to the substrate), as evidenced by the two main reflections at $2\theta = 14.2^{\circ}$ and $2\theta = 28.7^{\circ}$, which are ascribed to the (020) and (040) planes. The unit cell volumes derived from the whole-pattern Le Bail fits presented in Figure 2a are plotted in Figure 2b, showing a clear shrinkage of the unit cell from 831.5 $Å^3$ to 821 $Å^3$ as more iodide anions are replaced by bromide anions which have a smaller ionic radius (as well as FA^+ being replaced by Cs^+, though this replacement typically has a smaller effect in the lattice expansion or shrinkage than the anion-exchange). The different values obtained by the whole-pattern fits are the result of small shifts of the XRD peaks, which can be better visualized in Figure S9.

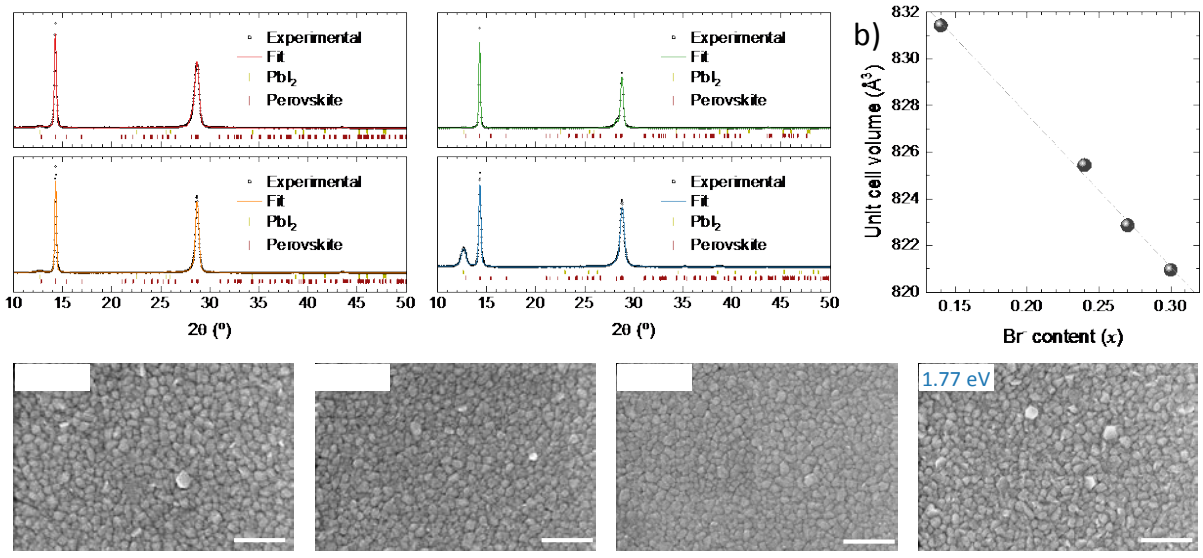

Figure 2. (a) Whole-pattern Le Bail fit (coloured lines) of XRD patterns (open black circles). Vertical markers correspond to calculated Bragg's reflections for a distorted perovskite phase (dark red) and PbI_2 (yellow). (b) Calculated unit cell volumes as obtained from fit as a function of the bromide content

estimated by EDS. (c) Surface morphology of the whole sample series as observed by SEM, scale bar corresponds to 500 nm.

We also studied the morphology of the $FA_{1-n}Cs_nPb(I_{1-x}Br_x)_3$ thin films by SEM top view images (Figure 2c). All films exhibit a similar surface morphology, composed of small grains (typical size in the 50-100 nm range) arranged in a compact and homogeneous manner. Such small grains are a common feature of vacuum deposited perovskite films, as highlighted in several previous reports.[82–84] The morphology of these materials is in stark contrast with what we have observed before for vacuum-deposited $Cs_{0.5}FA_{0.4}MA_{0.1}Pb(I_{0.83}Br_{0.17})_3$ films, obtained using CsBr as a simultaneous precursor for Cs^+ and Br^-.[73] As discussed in the introduction, that process does not allow to separately fine-tune the contents of the two ions (Cs^+ and Br^-), leading to irregular morphology with randomly oriented grains growing on the perovskite surface.

To shortly summarize, we demonstrated the successful room temperature deposition of highly oriented $FA_{1-n}Cs_nPb(I_{1-x}Br_x)_3$ films with homogeneous morphology and controlled and tunable bandgap from 1.70 eV to 1.77 eV. This is achieved with a 4-sources vacuum deposition process, using FAI, CsI, PbI_2 and $PbBr_2$ as the precursors. The use of $PbBr_2$ and CsI is important to control the relative bromide/cesium content in each sample, which are found stable against photoinduced halide segregation. In view of the favorable properties of the perovskite films presented above, we used them as the light-absorbing layer in fully vacuum-deposited perovskite solar cells. We fabricated p-i-n solar cells with the structure reported in Figure S10. Briefly, patterned indium tin oxide (ITO) transparent electrodes were coated with MoO_3 (5 nm) to enhance hole transfer between ITO and the hole transport layer (HTL), a 10 nm thick film of *N*4,*N*4,*N*4″,*N*4″-tetra([1,1′-biphenyl]-4-yl)-[1,1′:4′,1″-terphenyl]-4,4″-diamine (TaTm, 10 nm). Afterwards, a 500 nm thick perovskite film was deposited on top and capped with an electron transport layer (ETL, C_{60}, 25 nm). A thin (8 nm) film of bathocuproine (BCP) was used to ensure ohmic contact in between the ETL and a silver electrode (100 nm thick). Further details of the solar cell fabrication are reported in the Supporting Information.

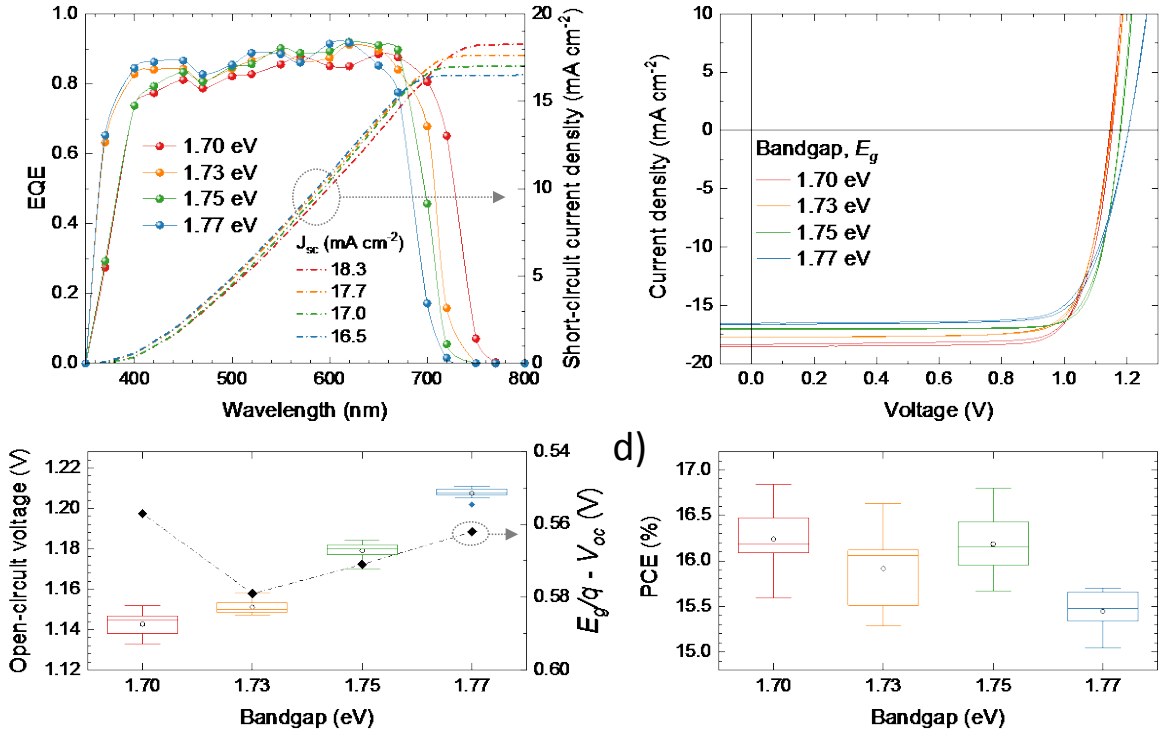

Figure 3. Characterization of wide-bandgap perovskite solar cells with $FA_{1-n}Cs_nPb(I_{1-x}Br_x)_3$ absorbers in p-i-n configuration. (a) External quantum efficiency (EQE) spectra (line and symbols) and corresponding short-circuit current density (J_{sc}, dotted lines) calculated by integration of each EQE spectrum with the global AM1.5G solar spectrum. (b) J-V curves under simulated solar illumination recorded in forward (from short to open circuit) and reverse (from open to short circuit) bias for representative pixels. Summary of the (c) open-circuit voltage (V_{oc}) and (d) power conversion efficiency (PCE) measured for perovskite solar cells as a function of the bandgap determined from Tauc analysis. In the right axis in (c), the open-circuit voltage deficit (E_g/q - V_{oc}) is also reported (lines are guides to the eye).

The external quantum efficiency (EQE, Figure 3a) spectra were found to be similarly high (in the 0.8 - 0.9 range) for the four materials through the whole visible spectrum. The onset of the spectral response in the low energy regime follows the trend expected from the perovskites optical absorption and bandgap (Figure 1), i.e. the EQE onset shifts to lower wavelengths when the content of bromide is increased. The corresponding short circuit currents (J_{sc}), calculated by integration of the EQE over the global AM1.5G solar spectra, decrease from 18.3 to 16.5 mA cm^{-2} when widening the bandgap from 1.70 eV to 1.77 eV. These values agree with those extracted from current-density vs. voltage (J-V) curves under simulated solar illumination, depicted in Figure 3b. The characteristic PV parameters

are reported in Table 1. All solar cells showed a high fill factor (FF, between 76 and 80 % on average), indicating an efficient charge extraction of the photogenerated charge carriers. We also observed negligible hysteresis in between the forward and reverse scans, which suggests that either ion migration or interface recombination (or both) are suppressed in these perovskite solar cells.[85,86] More interesting is the trend of the measured V_{oc}, which scales with the perovskite bandgap (Figure 3c), going on average from 1.14 V to 1.21 V for the 1.70 eV and 1.77 eV absorber, respectively going from 1.14 V for the 1.70 eV absorber to 1.21 V for the largest 1.77 eV bandgap, on average. The corresponding V_{oc} deficit, defined as (E_g/q-V_{oc}), was found to be rather large (0.56-0.58 V) and constant through the series of devices, indicating a common origin of the non-radiative recombination channels. Although far from the radiative limit for these semiconductors (see discussion below), these values are the highest voltages obtained for wide-bandgap mixed cation/halide perovskite solar cells deposited by vacuum deposition.

Table 1. Average photovoltaic parameters with standard deviation extracted from J-V curves under simulated solar illumination from wide-bandgap perovskite solar cells with $FA_{1-n}Cs_nPb(I_{1-x}Br_x)_3$ in p-i-n configuration. At least 12 cells for each bandgap have been tested.

Composition	*E_g (eV)*	*J_{sc} (mA cm^{-2})*	*FF (%)*	*V_{oc} (mV)*	*PCE (%)*
$FA_{0.74}Cs_{0.26}Pb(I_{0.86}Br_{0.14})_3$	1.70	18.3 ± 0.2	77.5 ± 0.9	1142 ± 6	16.2 ± 0.3
$FA_{0.71}Cs_{0.29}Pb(I_{0.76}Br_{0.24})_3$	1.73	17.7 ± 0.1	77.5 ± 1.2	1151 ± 3	15.9 ± 0.4
$FA_{0.65}Cs_{0.35}Pb(I_{0.73}Br_{0.27})_3$	1.75	17.0 ± 0.1	80.3 ± 0.8	1179 ± 4	16.2 ± 0.3
$FA_{0.61}Cs_{0.39}Pb(I_{0.70}Br_{0.30})_3$	1.77	16.6 ± 0.1	76.1 ± 0.8	1208 ± 2	15.5 ± 0.2

Overall, our wide-bandgap vacuum-deposited perovskite solar cells show PCEs of about 16% for bandgaps in the 1.70-1.75 eV range (Figure 3d). The best pixels were obtained for the wide-bandgap perovskite with E_g = 1.75 eV, with PCE up to 16.8% (Figure S11). The reduction in efficiency observed for the solar cells with the highest bromide content are partially expected due to the increased bandgap (1.77 eV), although a small decrease in FF also contributes to the efficiency reduction.

In order to further assess the quality of the wide-bandgap $FA_{1-n}Cs_nPb(I_{1-x}Br_x)_3$ perovskites and the corresponding solar cells, we investigated their EQE response in the bandgap region. From the semi-

logarithmic plot in **Figure 4**a one can see for all devices a steep drop of the EQE around the perovskite's bandgap.

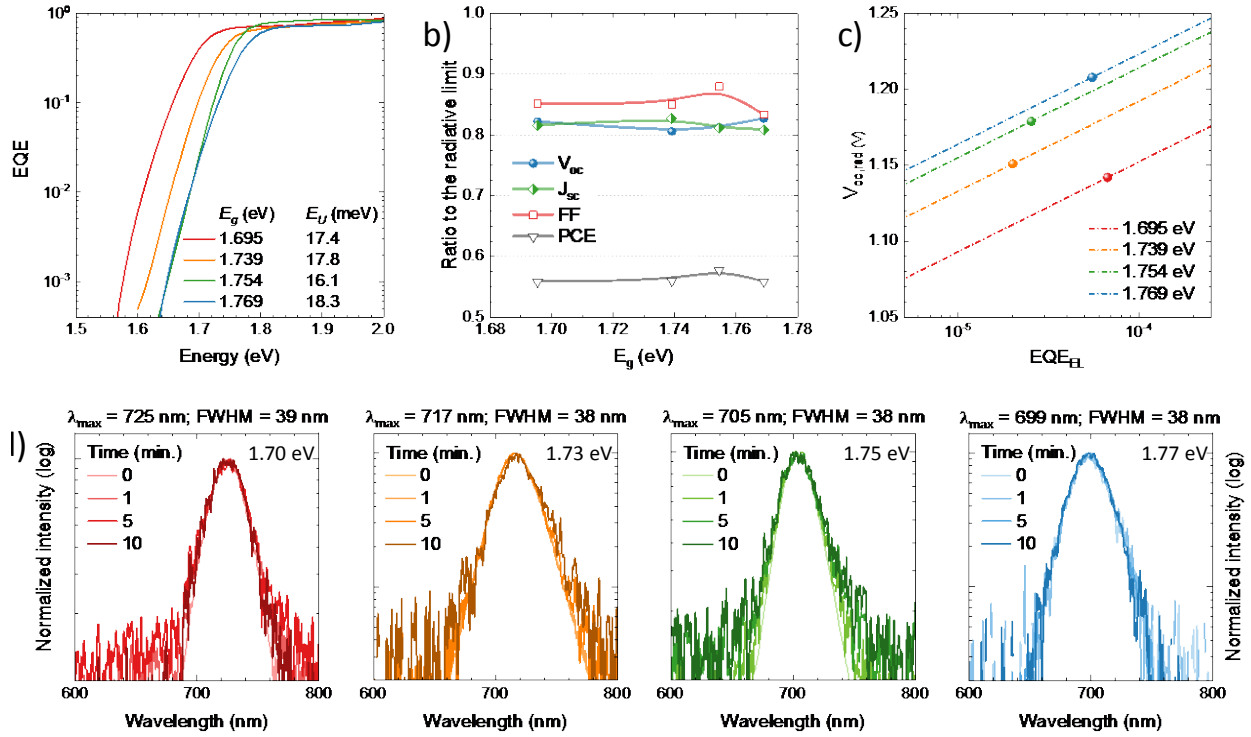

Figure 4. Optoelectronic analysis of $FA_{1-n}Cs_nPb(I_{1-x}Br_x)_3$ solar cells with different bandgaps. (a) Sensitive EQE spectra in the bandgap region and calculated bandgap and Urbach energies. (b) Ratio of measured V_{oc}, J_{sc} and FF to their maximum theoretical (radiative) limit (lines are guides to the eye). (c) Relation between the open-circuit voltage in the radiative limit with the PLQY of a solar cell (lines) for the four bandgaps studied here. Symbols shows the measured V_{oc}, allowing to estimate the corresponding PLQY. (d) Electroluminescence (EL) spectra of the same samples recorded over time (up to 10 minutes) under continuous forward bias. Each cell was driven with a constant current density equal to the J_{sc} obtained under simulated solar illumination.

From the slope we extracted the Urbach energies (E_U, see Supporting information for details), which are in the range of 16-18 meV, indicating a low electronic disorder that is essential to obtain high V_{oc}.[87] The bandgaps obtained from the derivative of the sensitive EQE measurements (Figure 4a) agree well with the values estimated from the Tauc plots in Figure 1b.[88] To be able to compare the limitations in performance of absorbers with different bandgap with each other, we divided the measured key performance indicators as obtained from the *J-V* curves by their maximal obtainable values in Figure 4b. The radiative limit of the V_{oc} ($V_{oc,rad}$) was calculated via the EQE response,[89] while the FF and J_{sc}

were obtained directly from detailed balance calculations given the specific bandgap of each material (Shockley-Queisser limit).[90,91] In general, all device parameters were found to be approximately at 80-90% of the theoretical maxima, highlighting the high quality of the perovskite films and devices reported here. The FF shows the highest ratio of the three parameters indicating good rectification and low series resistance. We noted that the solar cells prepared with the 1.75 eV perovskite showed consistently higher FF, which might originate from a larger charge carrier mobility for this particular composition. The J_{sc} and V_{oc} are more severely limiting the overall performance, with ratios only slightly above 80%. Interestingly, the $V_{oc}/V_{oc,rad}$ ratio rises marginally with the bandgap, in contrast to the commonly observed behaviour. This behaviour might be related with the increased amount of PbI_2 in the wider bandgap material as seen from XRD, which has been reported to passivate trap states in perovskite films.[92,93] However, the EQE of the electroluminescence (EQE_{EL}), estimated from the obtained photovoltage (Figure 4c, $EQE_{EL} = \exp(V_{oc}-V_{oc,rad})/kT)$), is in the 10^{-5} to 10^{-4} range for all devices, indicating the presence of non-radiative recombination either in the perovskite bulk or at the interface with the transport layers.[53–55] In order to shed light on the more relevant type of recombination, we evaluated the PL intensity of a perovskite film with and without the charge transport layers. As shown in Figure S13, the transport layers do quench the perovskite luminescence, indicating the presence of interface recombination. However, if we consider the relative PLQY obtained by integrating the PL spectra and normalizing it to the PL of the bare perovskite, we can estimate the QFLS difference in the presence of the transport materials. The difference in QFLS between the full stack (TaTm/perovskite/C_{60}) and a bare perovskite film is only about 50 mV. From this observation, and taking into account that the V_{oc} of a device is about 300 mV lower compared to its radiative limit, we can conclude that the V_{oc} is mainly limited by non-radiative recombination in the bulk of the perovskite layer. Hence future efforts should be directed towards passivation of such defect, through the use of additive or by modulating the deposition process. A possible loss pathway is the formation of iodide-rich domains driven by currents and electric fields, which would reduce the QFLS and hence the maximum attainable V_{oc}. It has been reported that even perovskite compositions which are stable under illumination, can show halide segregation under current injection, which is evidenced by the EL spectrum of the diodes.[94] Hence, we tested our series of perovskite solar cells in forward bias, applying a current density equivalent to their J_{sc}, and recorded the EL spectra as a function of time. Measurements are taken for up to 10 minutes as the EL intensity decreases over time (Figure S14) so that after 10-15 minutes the spectrometer cannot resolve the spectra anymore due to low signal-to-noise ratio. As highlighted in Figure 4d, the wide-bandgap solar cells were found to be very stable also under current injection, with the EL spectra showing a single component and no spectral changes over

time. The EL spectral positions are also in agreement with the PL signals depicted in Figure 1d. Therefore, we exclude halide segregation as a main loss factor.

We finally evaluated the stability of the most efficient solar cells based on $FA_{1-n}Cs_nPb(I_{1-x}Br_x)_3$ perovskites with E_g = 1.75 eV. Both the shelf life (in the dark) and the operational stability under illumination were evaluated. The devices were encapsulated with a UV-curable resin and a glass slide, and the stability was evaluated in a nitrogen atmosphere to minimize the effect of environmental factors on the degradation (note that no differences in performance were observed after encapsulation, see Figure S15). For the shelf-life stability, the *J-V* characteristics under 1-sun illumination were recorded periodically at room temperature (**Figure 5**a).

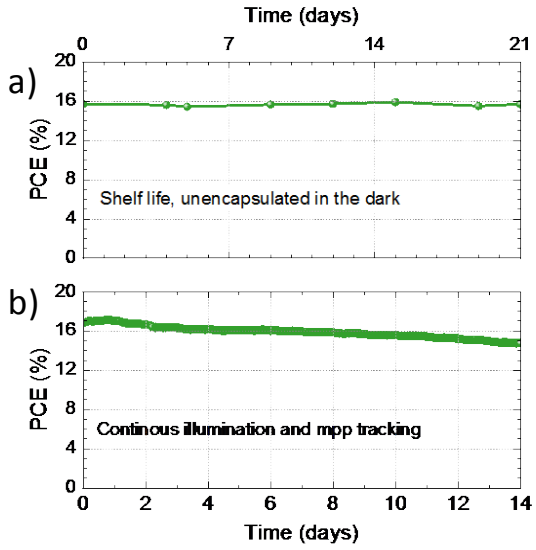

Figure 5. Stability assessment of wide-bandgap $FA_{0.65}Cs_{0.35}Pb(I_{0.73}Br_{0.27})_3$ perovskites solar cells with E_g = 1.75 eV, performed on encapsulated devices in nitrogen atmosphere. (a) Shelf-life measurements for devices kept in the dark. (b) Constant maximum power point tracking under continuous illumination.

After 500 hours of storage (3 weeks), the PCE was found unvaried from the initial value, indicating an overall good stability of the perovskite film within the device structure used here. To evaluate the operational stability, the devices were maintained at their maximum power point (MPP) under simulated 1-sun equivalent illumination with white LEDs at RT (25 ºC) in nitrogen (Figure 5b). Under these operational conditions the solar cell exhibited a remarkable stability, maintaining 90% of the initial PCE after 340 hours (more than 2 weeks) of continuous operation.

In summary, we showed the room temperature preparation of wide-bandgap perovskites films of the type $FA_{1-n}Cs_nPb(I_{1-x}Br_x)_3$ by thermal vacuum deposition. The simultaneous sublimation of four precursors, and in particular the use of $PbBr_2$ and CsI to individually control the bromide and cesium content, allows the deposition of wide-bandgap perovskites with bandgaps between 1.7 and 1.8 eV. In this way, no signatures of halide segregation and an overall homogeneous morphology can be attained. These film properties translate into efficient p-i-n solar cells, with photovoltaic parameters at 80% of their maximum theoretical (radiative) limits, highlighting the high quality of the as-deposited perovskite semiconductors. We obtained solar cells with bandgap of 1.75 eV and power conversion efficiency up to 16.8%. These devices retain 90% of their initial efficiency after more than 2 weeks of continuous operation. This work opens up the way towards the vacuum processing of photo-stable wide-bandgap perovskite solar cells for integration in tandem devices.

ASSOCIATED CONTENT

Supporting Information

The Supporting Information is available free of charge on the ACS Publications website at DOI: XXXX

Experimental methods, photoluminescence spectra analysis, XPS analysis, details of structural XRD analysis, device layout, details of calculation of bandgap, Urbach energy and radiative limit of the Voc from EQE measurements, time-dependent electroluminescence intensity.

ACKNOWLEDGEMENTS

The research leading to these results has received funding from the European Union's Horizon 2020 research and innovation programme under grant agreement No. 763977 of the PERTPV project, the Spanish Ministry of Science, Innovation and Universities (MICIU, MAT2017-88821-R, RTI2018-095362-A-I00, PCI2019-111829-2 and EQC2018-004888-P) and the Comunitat Valenciana (IDIFEDER/2018/061 and Prometeu/2020/077). C.D. acknowledges that the project that gave rise to these results received the support of a fellowship from "la Caixa" Foundation (ID 100010434, code LCF/BQ/DI19/11730020). M.S. and F.P. acknowledge the MICIU for their RyC and JdC contracts, respectively. S.A. acknowledges funding from the Federal Ministry of Education and Research (BMBF) for funding of the Young Investigator Group Perovskite Tandem Solar Cells within the

program “Materialforschung für die Energiewende” (grant no. 03SF0540), the Helmholtz Association within the HySPRINT Innovation lab project, and the HyPerCells Joint Graduate School. Z.H. and E.M. acknowledge SOLAR-ERA.NET and Swedish Energy Council (Energimyndigheten, contract 48381-1) for PERDRY project.

REFERENCES

(1) Snaith, H. J.; Hacke, P. Enabling Reliability Assessments of Pre-Commercial Perovskite Photovoltaics with Lessons Learned from Industrial Standards. *Nat. Energy* **2018**, *3* (6), 459–465. https://doi.org/10.1038/s41560-018-0174-4.

(2) Li, Z.; Klein, T. R.; Kim, D. H.; Yang, M.; Berry, J. J.; van Hest, M. F. A. M.; Zhu, K. Scalable Fabrication of Perovskite Solar Cells. *Nat. Rev. Mater.* **2018**, *3* (4), 18017. https://doi.org/10.1038/natrevmats.2018.17.

(3) Park, N.-G.; Grätzel, M.; Miyasaka, T.; Zhu, K.; Emery, K. Towards Stable and Commercially Available Perovskite Solar Cells. *Nat. Energy* **2016**, *1* (11), 16152. https://doi.org/10.1038/nenergy.2016.152.

(4) Dunlap-Shohl, W. A.; Zhou, Y.; Padture, N. P.; Mitzi, D. B. Synthetic Approaches for Halide Perovskite Thin Films. *Chem. Rev.* **2019**, *119* (5), 3193–3295. https://doi.org/10.1021/acs.chemrev.8b00318.

(5) Swartwout, R.; Hoerantner, M. T.; Bulović, V. Scalable Deposition Methods for Large-area Production of Perovskite Thin Films. *Energy Environ. Mater.* **2019**, *2* (2), 119–145. https://doi.org/10.1002/eem2.12043.

(6) Park, N.-G.; Zhu, K. Scalable Fabrication and Coating Methods for Perovskite Solar Cells and Solar Modules. *Nat. Rev. Mater.* **2020**, *5* (5), 333–350. https://doi.org/10.1038/s41578-019-0176-2.

(7) Yin, W.-J.; Shi, T.; Yan, Y. Unique Properties of Halide Perovskites as Possible Origins of the Superior Solar Cell Performance. *Adv. Mater.* **2014**, *26* (27), 4653–4658. https://doi.org/10.1002/adma.201306281.

(8) Chu, W.; Zheng, Q.; Prezhdo, O. V.; Zhao, J.; Saidi, W. A. Low-Frequency Lattice Phonons in Halide Perovskites Explain High Defect Tolerance toward Electron-Hole Recombination. *Sci. Adv.* **2020**, *6* (7), eaaw7453. https://doi.org/10.1126/sciadv.aaw7453.

(9) De Wolf, S.; Holovsky, J.; Moon, S.-J.; Löper, P.; Niesen, B.; Ledinsky, M.; Haug, F.-J.; Yum, J.-H.; Ballif, C. Organometallic Halide Perovskites: Sharp Optical Absorption Edge and Its Relation to Photovoltaic Performance. *J. Phys. Chem. Lett.* **2014**, *5* (6), 1035–1039. https://doi.org/10.1021/jz500279b.

(10) Adinolfi, V.; Yuan, M.; Comin, R.; Thibau, E. S.; Shi, D.; Saidaminov, M. I.; Kanjanaboos, P.; Kopilovic, D.; Hoogland, S.; Lu, Z.-H.; et al. The In-Gap Electronic State Spectrum of Methylammonium Lead Iodide Single-Crystal Perovskites. *Adv. Mater.* **2016**, *28* (17), 3406–3410. https://doi.org/10.1002/adma.201505162.

(11) Stranks, S. D.; Eperon, G. E.; Grancini, G.; Menelaou, C.; Alcocer, M. J. P.; Leijtens, T.; Herz, L. M.; Petrozza, A.; Snaith, H. J. Electron-Hole Diffusion Lengths Exceeding 1 Micrometer in an Organometal Trihalide Perovskite Absorber. *Science (80-.).* **2013**, *342* (6156), 341–344. https://doi.org/10.1126/science.1243982.

(12) Brenner, T. M.; Egger, D. A.; Kronik, L.; Hodes, G.; Cahen, D. Hybrid Organic—Inorganic Perovskites: Low-Cost Semiconductors with Intriguing Charge-Transport Properties. *Nat. Rev. Mater.* **2016**, *1* (1), 15007. https://doi.org/10.1038/natrevmats.2015.7.

(13) Huang, J.; Yuan, Y.; Shao, Y.; Yan, Y. Understanding the Physical Properties of Hybrid Perovskites for Photovoltaic Applications. *Nat. Rev. Mater.* **2017**, *2* (7), 17042. https://doi.org/10.1038/natrevmats.2017.42.

(14) Ball, J. M.; Petrozza, A. Defects in Perovskite-Halides and Their Effects in Solar Cells. *Nat. Energy* **2016**, *1* (11), 16149. https://doi.org/10.1038/nenergy.2016.149.

(15) Kojima, A.; Teshima, K.; Shirai, Y.; Miyasaka, T. Organometal Halide Perovskites as Visible-Light Sensitizers for Photovoltaic Cells. *J. Am. Chem. Soc.* **2009**, *131* (17), 6050–6051. https://doi.org/10.1021/ja809598r.

(16) Green, M. A.; Dunlop, E. D.; Hohl-Ebinger, J.; Yoshita, M.; Kopidakis, N.; Ho- Baillie, A. W. Y. Solar Cell Efficiency Tables (Version 55). *Prog. Photovoltaics Res. Appl.* **2020**, *28* (1), 3–15. https://doi.org/10.1002/pip.3228.

(17) Noh, J. H.; Im, S. H.; Heo, J. H.; Mandal, T. N.; Seok, S. Il. Chemical Management for Colorful, Efficient, and Stable Inorganic–Organic Hybrid Nanostructured Solar Cells. *Nano Lett.* **2013**, *13* (4), 1764–1769. https://doi.org/10.1021/nl400349b.

(18) Eperon, G. E.; Stranks, S. D.; Menelaou, C.; Johnston, M. B.; Herz, L. M.; Snaith, H. J.

Formamidinium Lead Trihalide: A Broadly Tunable Perovskite for Efficient Planar Heterojunction Solar Cells. *Energy Environ. Sci.* **2014**, *7* (3), 982. https://doi.org/10.1039/c3ee43822h.

(19) Protesescu, L.; Yakunin, S.; Bodnarchuk, M. I.; Krieg, F.; Caputo, R.; Hendon, C. H.; Yang, R. X.; Walsh, A.; Kovalenko, M. V. Nanocrystals of Cesium Lead Halide Perovskites (CsPbX 3 , X = Cl, Br, and I): Novel Optoelectronic Materials Showing Bright Emission with Wide Color Gamut. *Nano Lett.* **2015**, *15* (6), 3692–3696. https://doi.org/10.1021/nl5048779.

(20) Sutton, R. J.; Eperon, G. E.; Miranda, L.; Parrott, E. S.; Kamino, B. A.; Patel, J. B.; Hörantner, M. T.; Johnston, M. B.; Haghighirad, A. A.; Moore, D. T.; et al. Bandgap-Tunable Cesium Lead Halide Perovskites with High Thermal Stability for Efficient Solar Cells. *Adv. Energy Mater.* **2016**, *6* (8), 1–6. https://doi.org/10.1002/aenm.201502458.

(21) Eperon, G. E.; Hörantner, M. T.; Snaith, H. J. Metal Halide Perovskite Tandem and Multiple-Junction Photovoltaics. *Nat. Rev. Chem.* **2017**, *1* (12), 0095. https://doi.org/10.1038/s41570-017-0095.

(22) Leijtens, T.; Bush, K. A.; Prasanna, R.; McGehee, M. D. Opportunities and Challenges for Tandem Solar Cells Using Metal Halide Perovskite Semiconductors. *Nat. Energy* **2018**, *3* (10), 828–838. https://doi.org/10.1038/s41560-018-0190-4.

(23) Jošt, M.; Kegelmann, L.; Korte, L.; Albrecht, S. Monolithic Perovskite Tandem Solar Cells: A Review of the Present Status and Advanced Characterization Methods Toward 30% Efficiency. *Adv. Energy Mater.* **2020**, *10* (26), 1904102. https://doi.org/10.1002/aenm.201904102.

(24) Wang, Z.; Song, Z.; Yan, Y.; Liu, S. (Frank); Yang, D. Perovskite—a Perfect Top Cell for Tandem Devices to Break the S–Q Limit. *Adv. Sci.* **2019**, *6* (7), 1801704. https://doi.org/10.1002/advs.201801704.

(25) Han, Q.; Hsieh, Y.-T.; Meng, L.; Wu, J.-L.; Sun, P.; Yao, E.-P.; Chang, S.-Y.; Bae, S.-H.; Kato, T.; Bermudez, V.; et al. High-Performance Perovskite/Cu(In,Ga)Se 2 Monolithic Tandem Solar Cells. *Science (80-.).* **2018**, *361* (6405), 904–908. https://doi.org/10.1126/science.aat5055.

(26) Al-Ashouri, A.; Magomedov, A.; Roß, M.; Jošt, M.; Talaikis, M.; Chistiakova, G.; Bertram, T.; Márquez, J. A.; Köhnen, E.; Kasparavičius, E.; et al. Conformal Monolayer Contacts with

Lossless Interfaces for Perovskite Single Junction and Monolithic Tandem Solar Cells. *Energy Environ. Sci.* **2019**, *12* (11), 3356–3369. https://doi.org/10.1039/C9EE02268F.

(27) Kim, D. H.; Muzzillo, C. P.; Tong, J.; Palmstrom, A. F.; Larson, B. W.; Choi, C.; Harvey, S. P.; Glynn, S.; Whitaker, J. B.; Zhang, F.; et al. Bimolecular Additives Improve Wide-Band-Gap Perovskites for Efficient Tandem Solar Cells with CIGS. *Joule* **2019**, *3* (7), 1734–1745. https://doi.org/10.1016/j.joule.2019.04.012.

(28) Lang, F.; Jošt, M.; Frohna, K.; Köhnen, E.; Al-Ashouri, A.; Bowman, A. R.; Bertram, T.; Morales-Vilches, A. B.; Koushik, D.; Tennyson, E. M.; et al. Proton Radiation Hardness of Perovskite Tandem Photovoltaics. *Joule* **2020**, *4* (5), 1054–1069. https://doi.org/10.1016/j.joule.2020.03.006.

(29) Ko, E.; Macco, B.; Al-ashouri, A.; Korte, L. Environmental Science Textured Interfaces in Monolithic Perovskite / Silicon Tandem Solar Cells : Advanced Light Management for Improved Efficiency and Energy Yield †. **2018**, 3511–3523. https://doi.org/10.1039/c8ee02469c.

(30) Sahli, F.; Werner, J.; Kamino, B. A.; Bräuninger, M.; Monnard, R.; Paviet-Salomon, B.; Barraud, L.; Ding, L.; Diaz Leon, J. J.; Sacchetto, D.; et al. Fully Textured Monolithic Perovskite/Silicon Tandem Solar Cells with 25.2% Power Conversion Efficiency. *Nat. Mater.* **2018**, *17* (9), 820–826. https://doi.org/10.1038/s41563-018-0115-4.

(31) Kim, D.; Jung, H. J.; Park, I. J.; Larson, B. W.; Dunfield, S. P.; Xiao, C.; Kim, J.; Tong, J.; Boonmongkolras, P.; Ji, S. G.; et al. Efficient, Stable Silicon Tandem Cells Enabled by Anion-Engineered Wide-Bandgap Perovskites. *Science (80-.).* **2020**, *368* (6487), 155–160. https://doi.org/10.1126/science.aba3433.

(32) Chen, B.; Baek, S.-W.; Hou, Y.; Aydin, E.; De Bastiani, M.; Scheffel, B.; Proppe, A.; Huang, Z.; Wei, M.; Wang, Y.-K.; et al. Enhanced Optical Path and Electron Diffusion Length Enable High-Efficiency Perovskite Tandems. *Nat. Commun.* **2020**, *11* (1), 1257. https://doi.org/10.1038/s41467-020-15077-3.

(33) Xu, J.; Boyd, C. C.; Yu, Z. J.; Palmstrom, A. F.; Witter, D. J.; Larson, B. W.; France, R. M.; Werner, J.; Harvey, S. P.; Wolf, E. J.; et al. Triple-Halide Wide–Band Gap Perovskites with Suppressed Phase Segregation for Efficient Tandems. *Science (80-.).* **2020**, *367* (6482), 1097–1104. https://doi.org/10.1126/science.aaz5074.

(34) Hou, Y.; Aydin, E.; De Bastiani, M.; Xiao, C.; Isikgor, F. H.; Xue, D.-J.; Chen, B.; Chen, H.; Bahrami, B.; Chowdhury, A. H.; et al. Efficient Tandem Solar Cells with Solution-Processed Perovskite on Textured Crystalline Silicon. *Science (80-.).* **2020**, *367* (6482), 1135–1140. https://doi.org/10.1126/science.aaz3691.

(35) Coletti, G.; Luxembourg, S. L.; Geerligs, L. J.; Rosca, V.; Burgers, A. R.; Wu, Y.; Okel, L.; Kloos, M.; Danzl, F. J. K.; Najafi, M.; et al. Bifacial Four-Terminal Perovskite/Silicon Tandem Solar Cells and Modules. *ACS Energy Lett.* **2020**, *5* (5), 1676–1680. https://doi.org/10.1021/acsenergylett.0c00682.

(36) Eperon, G. E.; Leijtens, T.; Bush, K. A.; Prasanna, R.; Green, T.; Wang, J. T.-W.; McMeekin, D. P.; Volonakis, G.; Milot, R. L.; May, R.; et al. Perovskite-Perovskite Tandem Photovoltaics with Optimized Band Gaps. *Science (80-.).* **2016**, *354* (6314), 861–865. https://doi.org/10.1126/science.aaf9717.

(37) Forgács, D.; Gil-Escrig, L.; Pérez-Del-Rey, D.; Momblona, C.; Werner, J.; Niesen, B.; Ballif, C.; Sessolo, M.; Bolink, H. J. Efficient Monolithic Perovskite/Perovskite Tandem Solar Cells. *Adv. Energy Mater.* **2017**, *7* (8), 1602121. https://doi.org/10.1002/aenm.201602121.

(38) Zhao, D.; Chen, C.; Wang, C.; Junda, M. M.; Song, Z.; Grice, C. R.; Yu, Y.; Li, C.; Subedi, B.; Podraza, N. J.; et al. Efficient Two-Terminal All-Perovskite Tandem Solar Cells Enabled by High-Quality Low-Bandgap Absorber Layers. *Nat. Energy* **2018**, *3* (12), 1093–1100. https://doi.org/10.1038/s41560-018-0278-x.

(39) Palmstrom, A. F.; Eperon, G. E.; Leijtens, T.; Prasanna, R.; Habisreutinger, S. N.; Nemeth, W.; Gaulding, E. A.; Dunfield, S. P.; Reese, M.; Nanayakkara, S.; et al. Enabling Flexible All-Perovskite Tandem Solar Cells. *Joule* **2019**, *3* (9), 2193–2204. https://doi.org/10.1016/j.joule.2019.05.009.

(40) Yang, Z.; Yu, Z.; Wei, H.; Xiao, X.; Ni, Z.; Chen, B.; Deng, Y.; Habisreutinger, S. N.; Chen, X.; Wang, K.; et al. Enhancing Electron Diffusion Length in Narrow-Bandgap Perovskites for Efficient Monolithic Perovskite Tandem Solar Cells. *Nat. Commun.* **2019**, *10* (1), 1–9. https://doi.org/10.1038/s41467-019-12513-x.

(41) Lin, R.; Xiao, K.; Qin, Z.; Han, Q.; Zhang, C.; Wei, M.; Saidaminov, M. I.; Gao, Y.; Xu, J.; Xiao, M.; et al. Monolithic All-Perovskite Tandem Solar Cells with 24.8% Efficiency Exploiting Comproportionation to Suppress Sn(Ii) Oxidation in Precursor Ink. *Nat. Energy* **2019**, *4* (10), 864–873. https://doi.org/10.1038/s41560-019-0466-3.

(42) Tong, J.; Song, Z.; Kim, D. H.; Chen, X.; Chen, C.; Palmstrom, A. F.; Ndione, P. F.; Reese, M. O.; Dunfield, S. P.; Reid, O. G.; et al. Carrier Lifetimes of >1 Ms in Sn-Pb Perovskites Enable Efficient All-Perovskite Tandem Solar Cells. *Science (80-.).* **2019**, *364* (6439), 475–479. https://doi.org/10.1126/science.aav7911.

(43) Hao, F.; Stoumpos, C. C.; Chang, R. P. H.; Kanatzidis, M. G. Anomalous Band Gap Behavior in Mixed Sn and Pb Perovskites Enables Broadening of Absorption Spectrum in Solar Cells. *J. Am. Chem. Soc.* **2014**, *136* (22), 8094–8099. https://doi.org/10.1021/ja5033259.

(44) Prasanna, R.; Gold-Parker, A.; Leijtens, T.; Conings, B.; Babayigit, A.; Boyen, H.-G.; Toney, M. F.; McGehee, M. D. Band Gap Tuning via Lattice Contraction and Octahedral Tilting in Perovskite Materials for Photovoltaics. *J. Am. Chem. Soc.* **2017**, *139* (32), 11117–11124. https://doi.org/10.1021/jacs.7b04981.

(45) Hoke, E. T.; Slotcavage, D. J.; Dohner, E. R.; Bowring, A. R.; Karunadasa, H. I.; McGehee, M. D. Reversible Photo-Induced Trap Formation in Mixed-Halide Hybrid Perovskites for Photovoltaics. *Chem. Sci.* **2015**, *6* (1), 613–617. https://doi.org/10.1039/C4SC03141E.

(46) McMeekin, D. P.; Sadoughi, G.; Rehman, W.; Eperon, G. E.; Saliba, M.; Horantner, M. T.; Haghighirad, A.; Sakai, N.; Korte, L.; Rech, B.; et al. A Mixed-Cation Lead Mixed-Halide Perovskite Absorber for Tandem Solar Cells. *Science (80-.).* **2016**, *351* (6269), 151–155. https://doi.org/10.1126/science.aad5845.

(47) Bush, K. A.; Frohna, K.; Prasanna, R.; Beal, R. E.; Leijtens, T.; Swifter, S. A.; McGehee, M. D. Compositional Engineering for Efficient Wide Band Gap Perovskites with Improved Stability to Photoinduced Phase Segregation. *ACS Energy Lett.* **2018**, *3* (2), 428–435. https://doi.org/10.1021/acsenergylett.7b01255.

(48) Yang, T. C.-J.; Fiala, P.; Jeangros, Q.; Ballif, C. High-Bandgap Perovskite Materials for Multijunction Solar Cells. *Joule* **2018**, *2* (8), 1421–1436. https://doi.org/10.1016/j.joule.2018.05.008.

(49) Gharibzadeh, S.; Abdollahi Nejand, B.; Jakoby, M.; Abzieher, T.; Hauschild, D.; Moghadamzadeh, S.; Schwenzer, J. A.; Brenner, P.; Schmager, R.; Haghighirad, A. A.; et al. Record Open-Circuit Voltage Wide- Bandgap Perovskite Solar Cells Utilizing 2D/3D Perovskite Heterostructure. *Adv. Energy Mater.* **2019**, *9* (21), 1803699. https://doi.org/10.1002/aenm.201803699.

(50) Rajagopal, A.; Stoddard, R. J.; Jo, S. B.; Hillhouse, H. W.; Jen, A. K. Y. Overcoming the Photovoltage Plateau in Large Bandgap Perovskite Photovoltaics. *Nano Lett.* **2018**, *18* (6), 3985–3993. https://doi.org/10.1021/acs.nanolett.8b01480.

(51) Peña-Camargo, F.; Caprioglio, P.; Zu, F.; Gutierrez-Partida, E.; Wolff, C. M.; Brinkmann, K.; Albrecht, S.; Riedl, T.; Koch, N.; Neher, D.; et al. Halide Segregation versus Interfacial Recombination in Bromide-Rich Wide-Gap Perovskite Solar Cells. *ACS Energy Lett.* **2020**, *5* (8), 2728–2736. https://doi.org/10.1021/acsenergylett.0c01104.

(52) Liu, Z.; Krückemeier, L.; Krogmeier, B.; Klingebiel, B.; Márquez, J. A.; Levcenko, S.; Öz, S.; Mathur, S.; Rau, U.; Unold, T.; et al. Open-Circuit Voltages Exceeding 1.26 V in Planar Methylammonium Lead Iodide Perovskite Solar Cells. *ACS Energy Lett.* **2019**, *4* (1), 110–117. https://doi.org/10.1021/acsenergylett.8b01906.

(53) Wolff, C. M.; Caprioglio, P.; Stolterfoht, M.; Neher, D. Nonradiative Recombination in Perovskite Solar Cells: The Role of Interfaces. *Adv. Mater.* **2019**, *31* (52), 1902762. https://doi.org/10.1002/adma.201902762.

(54) deQuilettes, D. W.; Frohna, K.; Emin, D.; Kirchartz, T.; Bulovic, V.; Ginger, D. S.; Stranks, S. D. Charge-Carrier Recombination in Halide Perovskites. *Chem. Rev.* **2019**, *119* (20), 11007–11019. https://doi.org/10.1021/acs.chemrev.9b00169.

(55) Mahesh, S.; Ball, J. M.; Oliver, R. D. J.; McMeekin, D. P.; Nayak, P. K.; Johnston, M. B.; Snaith, H. J. Revealing the Origin of Voltage Loss in Mixed-Halide Perovskite Solar Cells. *Energy Environ. Sci.* **2020**, *13* (1), 258–267. https://doi.org/10.1039/C9EE02162K.

(56) Aydin, E.; Bastiani, M.; Wolf, S. Defect and Contact Passivation for Perovskite Solar Cells. *Adv. Mater.* **2019**, *31* (25), 1900428. https://doi.org/10.1002/adma.201900428.

(57) Kim, J.; Ho-Baillie, A.; Huang, S. Review of Novel Passivation Techniques for Efficient and Stable Perovskite Solar Cells. *Sol. RRL* **2019**, *3* (4), 1800302. https://doi.org/10.1002/solr.201800302.

(58) Gao, F.; Zhao, Y.; Zhang, X.; You, J. Recent Progresses on Defect Passivation toward Efficient Perovskite Solar Cells. *Adv. Energy Mater.* **2020**, *10* (13), 1902650. https://doi.org/10.1002/aenm.201902650.

(59) Akin, S.; Arora, N.; Zakeeruddin, S. M.; Grätzel, M.; Friend, R. H.; Dar, M. I. New Strategies for Defect Passivation in High-Efficiency Perovskite Solar Cells. *Adv. Energy Mater.* **2020**,

10 (13), 1903090. https://doi.org/10.1002/aenm.201903090.

(60) Chen, B.; Rudd, P. N.; Yang, S.; Yuan, Y.; Huang, J. Imperfections and Their Passivation in Halide Perovskite Solar Cells. *Chem. Soc. Rev.* **2019**, *48* (14), 3842–3867. https://doi.org/10.1039/C8CS00853A.

(61) Lin, Q.; Armin, A.; Nagiri, R. C. R.; Burn, P. L.; Meredith, P. Electro-Optics of Perovskite Solar Cells. *Nat. Photonics* **2015**, *9* (2), 106–112. https://doi.org/10.1038/nphoton.2014.284.

(62) Hsiao, S.-Y.; Lin, H.-L.; Lee, W.-H.; Tsai, W.-L.; Chiang, K.-M.; Liao, W.-Y.; Ren-Wu, C.-Z.; Chen, C.-Y.; Lin, H.-W. Efficient All-Vacuum Deposited Perovskite Solar Cells by Controlling Reagent Partial Pressure in High Vacuum. *Adv. Mater.* **2016**, *28* (32), 7013–7019. https://doi.org/10.1002/adma.201601505.

(63) Li, J.; Wang, H.; Chin, X. Y.; Dewi, H. A.; Vergeer, K.; Goh, T. W.; Lim, J. W. M.; Lew, J. H.; Loh, K. P.; Soci, C.; et al. Highly Efficient Thermally Co-Evaporated Perovskite Solar Cells and Mini-Modules. *Joule* **2020**, *4* (5), 1035–1053. https://doi.org/10.1016/j.joule.2020.03.005.

(64) Ávila, J.; Momblona, C.; Boix, P.; Sessolo, M.; Anaya, M.; Lozano, G.; Vandewal, K.; Míguez, H.; Bolink, H. J. High Voltage Vacuum-Deposited CH 3 NH 3 PbI 3 –CH 3 NH 3 PbI 3 Tandem Solar Cells. *Energy Environ. Sci.* **2018**, *11* (11), 3292–3297. https://doi.org/10.1039/C8EE01936C.

(65) Liu, M.; Johnston, M. B.; Snaith, H. J. Efficient Planar Heterojunction Perovskite Solar Cells by Vapour Deposition. *Nature* **2013**, *501* (7467), 395–398. https://doi.org/10.1038/nature12509.

(66) Malinkiewicz, O.; Yella, A.; Lee, Y. H.; Espallargas, G. M.; Graetzel, M.; Nazeeruddin, M. K.; Bolink, H. J. Perovskite Solar Cells Employing Organic Charge-Transport Layers. *Nat. Photonics* **2014**, *8* (2), 128–132. https://doi.org/10.1038/nphoton.2013.341.

(67) Momblona, C.; Gil-Escrig, L.; Bandiello, E.; Hutter, E. M.; Sessolo, M.; Lederer, K.; Blochwitz-Nimoth, J.; Bolink, H. J. Efficient Vacuum Deposited P-i-n and n-i-p Perovskite Solar Cells Employing Doped Charge Transport Layers. *Energy Environ. Sci.* **2016**, *9* (11), 3456–3463. https://doi.org/10.1039/C6EE02100J.

(68) Al-Ashouri, A.; Magomedov, A.; Roß, M.; Jošt, M.; Talaikis, M.; Chistiakova, G.; Bertram, T.; Márquez, J. A.; Köhnen, E.; Kasparavičius, E.; et al. Conformal Monolayer Contacts with

Lossless Interfaces for Perovskite Single Junction and Monolithic Tandem Solar Cells. *Energy Environ. Sci.* **2019**, *12* (11), 3356–3369. https://doi.org/10.1039/C9EE02268F.

(69) Longo, G.; Momblona, C.; La-Placa, M.-G.; Gil-Escrig, L.; Sessolo, M.; Bolink, H. J. Fully Vacuum-Processed Wide Band Gap Mixed-Halide Perovskite Solar Cells. *ACS Energy Lett.* **2018**, *3* (1), 214–219. https://doi.org/10.1021/acsenergylett.7b01217.

(70) Slotcavage, D. J.; Karunadasa, H. I.; McGehee, M. D. Light-Induced Phase Segregation in Halide-Perovskite Absorbers. *ACS Energy Lett.* **2016**, *1* (6), 1199–1205. https://doi.org/10.1021/acsenergylett.6b00495.

(71) Knight, A. J.; Herz, L. M. Preventing Phase Segregation in Mixed-Halide Perovskites: A Perspective. *Energy Environ. Sci.* **2020**, *13* (7), 2024–2046. https://doi.org/10.1039/D0EE00788A.

(72) Huang, J.; Xiang, S.; Yu, J.; Li, C.-Z. Highly Efficient Prismatic Perovskite Solar Cells. *Energy Environ. Sci.* **2019**, *12* (3), 929–937. https://doi.org/10.1039/C8EE02575D.

(73) Gil-Escrig, L.; Momblona, C.; La-Placa, M.-G.; Boix, P. P.; Sessolo, M.; Bolink, H. J. Vacuum Deposited Triple-Cation Mixed-Halide Perovskite Solar Cells. *Adv. Energy Mater.* **2018**, *8* (14), 1703506. https://doi.org/10.1002/aenm.201703506.

(74) Ji, R.; Zhang, Z.; Cho, C.; An, Q.; Paulus, F.; Kroll, M.; Löffler, M.; Nehm, F.; Rellinghaus, B.; Leo, K.; et al. Thermally Evaporated Methylammonium-Free Perovskite Solar Cells. *J. Mater. Chem. C* **2020**, *8* (23), 7725–7733. https://doi.org/10.1039/D0TC01550D.

(75) Chiang, Y.; Anaya, M.; Stranks, S. D. Multisource Vacuum Deposition of Methylammonium-Free Perovskite Solar Cells. *ACS Energy Lett.* **2020**, *5* (8), 2498–2504. https://doi.org/10.1021/acsenergylett.0c00839.

(76) Kim, B.-S.; Gil-Escrig, L.; Sessolo, M.; Bolink, H. J. Deposition Kinetics and Compositional Control of Vacuum-Processed CH 3 NH 3 PbI 3 Perovskite. *J. Phys. Chem. Lett.* **2020**, *11* (16), 6852–6859. https://doi.org/10.1021/acs.jpclett.0c01995.

(77) Gil-Escrig, L.; Dreessen, C.; Kaya, I. C.; Kim, B.-S.; Palazon, F.; Sessolo, M.; Bolink, H. J. Efficient Vacuum-Deposited Perovskite Solar Cells with Stable Cubic FA 1– x MA x PbI 3. *ACS Energy Lett.* **2020**, 3053–3061. https://doi.org/10.1021/acsenergylett.0c01473.

(78) Scofield, J. H. Hartree-Slater Subshell Photoionization Cross-Sections at 1254 and 1487 EV. *J. Electron Spectros. Relat. Phenomena* **1976**, *8* (2), 129–137. https://doi.org/10.1016/0368-

2048(76)80015-1.

(79) Seah, M. P.; Dench, W. A. Quantitative Electron Spectroscopy of Surfaces: A Standard Data Base for Electron Inelastic Mean Free Paths in Solids. *Surf. Interface Anal.* **1979**, *1* (1), 2–11. https://doi.org/10.1002/sia.740010103.

(80) Goldstein, J. I.; Newbury, D. E.; Michael, J. R.; Ritchie, N. W. M.; Scott, J. H. J.; Joy, D. C. Qualitative Elemental Analysis by Energy Dispersive X-Ray Spectrometry. In *Scanning Electron Microscopy and X-Ray Microanalysis*; Springer New York: New York, NY, 2018; pp 265–287. https://doi.org/10.1007/978-1-4939-6676-9_18.

(81) Akkerman, Q. A.; Manna, L. What Defines a Halide Perovskite? *ACS Energy Lett.* **2020**, 604–610. https://doi.org/10.1021/acsenergylett.0c00039.

(82) Momblona, C.; Gil-Escrig, L.; Bandiello, E.; Hutter, E. M.; Sessolo, M.; Lederer, K.; Blochwitz-Nimoth, J.; Bolink, H. J. Efficient Vacuum Deposited P-i-n and n-i-p Perovskite Solar Cells Employing Doped Charge Transport Layers. *Energy Environ. Sci.* **2016**, *9* (11), 3456–3463. https://doi.org/10.1039/C6EE02100J.

(83) Roß, M.; Gil-Escrig, L.; Al-Ashouri, A.; Tockhorn, P.; Jošt, M.; Rech, B.; Albrecht, S. Co-Evaporated p-i-n Perovskite Solar Cells beyond 20% Efficiency: Impact of Substrate Temperature and Hole-Transport Layer. *ACS Appl. Mater. Interfaces* **2020**, *12* (35), 39261–39272. https://doi.org/10.1021/acsami.0c10898.

(84) Lohmann, K. B.; Patel, J. B.; Rothmann, M. U.; Xia, C. Q.; Oliver, R. D. J.; Herz, L. M.; Snaith, H. J.; Johnston, M. B. Control over Crystal Size in Vapor Deposited Metal-Halide Perovskite Films. *ACS Energy Lett.* **2020**, *5* (3), 710–717. https://doi.org/10.1021/acsenergylett.0c00183.

(85) van Reenen, S.; Kemerink, M.; Snaith, H. J. Modeling Anomalous Hysteresis in Perovskite Solar Cells. *J. Phys. Chem. Lett.* **2015**, *6* (19), 3808–3814. https://doi.org/10.1021/acs.jpclett.5b01645.

(86) Calado, P.; Telford, A. M.; Bryant, D.; Li, X.; Nelson, J.; O'Regan, B. C.; Barnes, P. R. F. Evidence for Ion Migration in Hybrid Perovskite Solar Cells with Minimal Hysteresis. *Nat. Commun.* **2016**, *7* (1), 13831. https://doi.org/10.1038/ncomms13831.

(87) Chantana, J.; Kawano, Y.; Nishimura, T.; Mavlonov, A.; Minemoto, T. Impact of Urbach Energy on Open-Circuit Voltage Deficit of Thin-Film Solar Cells. *Sol. Energy Mater. Sol.*

Cells **2020**, *210* (January), 110502. https://doi.org/10.1016/j.solmat.2020.110502.

(88) Rau, U.; Blank, B.; Müller, T. C. ~M.; Kirchartz, T. Efficiency Potential of Photovoltaic Materials and Devices Unveiled by Detailed-Balance Analysis. *Phys. Rev. Appl.* **2017**, *7* (4), 44016. https://doi.org/10.1103/PhysRevApplied.7.044016.

(89) Rau, U. Reciprocity Relation between Photovoltaic Quantum Efficiency and Electroluminescent Emission of Solar Cells. *Phys. Rev. B* **2007**, *76* (8), 85303. https://doi.org/10.1103/PhysRevB.76.085303.

(90) Shockley, W.; Queisser, H. J. Detailed Balance Limit of Efficiency of P-n Junction Solar Cells. *J. Appl. Phys.* **1961**, *32* (3), 510–519. https://doi.org/10.1063/1.1736034.

(91) Rühle, S. Tabulated Values of the Shockley–Queisser Limit for Single Junction Solar Cells. *Sol. Energy* **2016**, *130*, 139–147. https://doi.org/10.1016/j.solener.2016.02.015.

(92) Chen, Q.; Zhou, H.; Song, T.-B.; Luo, S.; Hong, Z.; Duan, H.-S.; Dou, L.; Liu, Y.; Yang, Y. Controllable Self-Induced Passivation of Hybrid Lead Iodide Perovskites toward High Performance Solar Cells. *Nano Lett.* **2014**, *14* (7), 4158–4163. https://doi.org/10.1021/nl501838y.

(93) Lee, J.-W.; Kim, S.-G.; Bae, S.-H.; Lee, D.-K.; Lin, O.; Yang, Y.; Park, N.-G. The Interplay between Trap Density and Hysteresis in Planar Heterojunction Perovskite Solar Cells. *Nano Lett.* **2017**, *17* (7), 4270–4276. https://doi.org/10.1021/acs.nanolett.7b01211.

(94) Braly, I. L.; Stoddard, R. J.; Rajagopal, A.; Uhl, A. R.; Katahara, J. K.; Jen, A. K. Y.; Hillhouse, H. W. Current-Induced Phase Segregation in Mixed Halide Hybrid Perovskites and Its Impact on Two-Terminal Tandem Solar Cell Design. *ACS Energy Lett.* **2017**, *2* (8), 1841–1847. https://doi.org/10.1021/acsenergylett.7b00525.

SUPPORTING INFORMATION

Efficient wide-bandgap mixed-cation and mixed-halide perovskite solar cells by vacuum deposition

Lidón Gil-Escrig,[a] Chris Dreessen,[a] Francisco Palazon,[a] Zafer Hawash,[b] Ellen Moons,[b] Steve Albrecht,[c] Michele Sessolo [a,*] and Henk J. Bolink[a]

[a]*Instituto de Ciencia Molecular, Universidad de Valencia, C/ Catedrático J. Beltrán 2, 46980, Paterna, Spain. E-mail:* michele.sessolo@uv.es

[b]*Department of Physics, Karlstad University, SE-65188 Karlstad, Sweden*

[c]*Young Investigator Group for Perovskite Tandem Solar Cells, Helmholtz-Center Berlin, Kekuléstrasse 5, 12489 Berlin, Germany*

Materials. *N4,N4,N4‘,N4‘*-tetra([1,1‘-biphenyl]-4-yl)-[1,1‘:4‘,1‘-terphenyl]-4,4‘-diamine (TaTm) was provided by Novaled GmbH and fullerene (C_{60}) was purchased from Merck KGaA. PbI_2, CH_3NH_3I (MAI), MoO_3, and bathocuproine (BCP) were purchased from Luminescence Technology Corp. $CHNH_2NH_2I$ (FAI) was purchased from Greatcell Solar. $PbBr_2$ was obtained from Tokyo Chemical Industry. All materials were used as received.

Device preparation. ITO-coated glass substrates were subsequently cleaned with soap, water and isopropanol in an ultrasonic bath, followed by 20 min UV-ozone treatment. The substrates were transferred to a vacuum chamber integrated in a nitrogen-filled glovebox and evacuated to a pressure of 10^{-6} mbar for the charge extraction layers’ deposition. In general, the deposition rate for the TaTm and C_{60} was 0.5 Å/s while the thinner BCP layer was sublimed at 0.2 Å/s. MoO_3 and Ag were deposited in a second vacuum chamber using aluminum boats as sources, by applying currents ranging from 2.0 to 4.5 A. The perovskite was evaporated in another vacuum chamber, equipped with four evaporation sources (Creaphys) and with independent temperature controllers and shutters. All sources have a dedicated QCM sensor above, and an additional one is installed close to the substrates for the overall deposition rate measurement. All sources were individually calibrated for their respective materials and no cross-reading between different materials is ensured by the position of the sources, shutters, sensors. During the $FA_{1-n}Cs_nPb(I_{1-x}Br_x)_3$ perovskite deposition, the FAI and PbI_2 deposition rates were kept constant at 0.8 Å/s and 1 Å/s, respectively. In order to tune the bandgap while ensuring phase stability, $PbBr_2$ and CsI

were sublimed at varying deposition rates, in the range of 0.25-0.45 Å/s and 0.07-0.22 Å/s, respectively. During the perovskite deposition, the pressure of the chamber was mantained at $8 \cdot 10^{-6}$ mbar and the substrates were kept at room temperature. Typical sublimation temperatures for the precursors were 150 ºC for FAI, 310 ºC for PbI_2, 280-300 ºC for $PbBr_2$ and 490 - 520ºC for CsI.

Characterization. Absorption spectra were collected using fiber optics based Avantes Avaspec2048 Spectrometer. The photoluminescence spectra were measured with an Avantes Avaspec2048 spectrometer and films were illuminated with a diode laser of integrated optics, emitting at 522 nm. All the spectra were collected with an integration time of 1 s. The crystalline structure of the powder and film samples was studied by X-ray diffraction (XRD). The patterns were collected in Bragg-Brentano geometry on an Empyrean PANalytical powder diffractometer with a copper anode operated at 45 kV and 40 mA. Further analysis including Le Bail fits were performed with Fullprof software. Scanning Electron Microscopy (SEM) images were performed on a Hitachi S-4800 microscope operating at an accelerating voltage of 2 kV over platinum-metallized samples.

High resolution x-ray photoemission spectroscopy (XPS, Sceinta Omicron SES-100, non-monochromatic Al−Kα = 1486.6 eV) measurements were performed to quantify the chemical composition of the top surface of the perovskite film. The peak fitting and atomic percentage calculations were performed using CasaXPS 2.3.16 software. Shirley background lines and gaussian-lorentzian shape lines were used for fitting the components. The binding energy (BE) for XPS was calibrated by measuring Fermi edge (E_F = 0 eV) and Au-$4f_{7/2}$ (84.0 eV) on a clean Au surface. The x-ray gun was operated at 250W. The estimated energy resolution of XPS is 0.7 eV. XPS measurements were performed in an ultra-high vacuum (UHV) chamber with pressure of about 1×10^{-10} mbar. The acquisition was performed with pass energy of 20 eV and dwell time of 0.1 sec. X-ray-induced sample damage was monitored by taking several consecutive spectra and comparing those spectra. In case of no damage observed, all the collected spectra for each core level were averaged into the final high resolution spectrum. Time acquisition for each scan varied from 40 to 70 sec depending on the core level region. To minimize any possible unnecessary x-ray exposure time, special care was taken while optimizing and acquiring XPS measurements. No X-ray-induced damage was observed on the films. All the calculated atomic percentages are normalised according to Hartree-Slater Subshell Photoionization Cross-Sections at 1486.6 eV.[1]

The J-V curves for the solar cells were recorded using a Keithley 2612A SourceMeter in a -0.2 and 1.3 V voltage range, with 0.01 V steps and integrating the signal for 20 ms after a 10 ms delay, corresponding to a scan speed of about 0.3 Vs^{-1}. The devices were illuminated under a

Wavelabs Sinus 70 LED solar simulator. The light intensity was calibrated before every measurement using a calibrated Si reference diode. The external quantum efficiency (EQE) was estimated using the cell response at different wavelength (measured with a white light halogen lamp in combination with band-pass filters), where the solar spectrum mismatch was corrected with a calibrated Silicon reference cell (MiniSun simulator by ECN, from Netherlands).

For the sensitive EQE measurements, the cell was illuminated by a Quartz-Tungsten- Halogen lamp (Newport Apex 2-QTH) thro ugh a monochromator (Newport CS130-USB- 3- MC), a chopper at 279 Hz and a focusing lens. The device current was measured as a function of energy from 2.1 eV to 1.2 eV in 0.02 eV steps using a lock-in amplifier (Stanford Research Systems SR830). The system was calibrated and the solar spectrum mismatch was corrected using a calibrated Silicon reference cell.

Solar cell stability measurements were recorded using a maximum power point tracker (mppt) system, with a white LED light source under 1 sun equivalent, developed by Candlelight. During the mppt measurements, a flow of N_2 gas was used and temperature was kept at 300 K using a water-circulating cooling system.

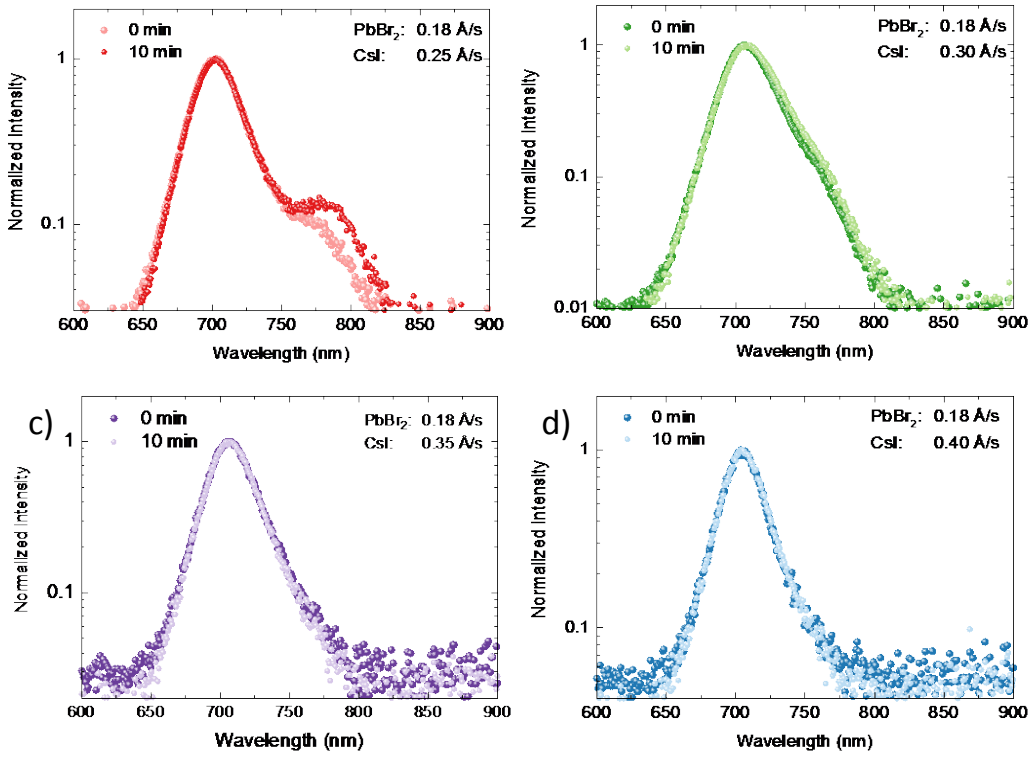

Figure S1. Photoluminescence (PL) spectra in semi-logarithmic scale under laser excitation (515 nm), at time 0 and after 10 minutes of continuous irradiation, for perovskite films with bandgap of approximately 1.75 eV (Br- content, $x = 0.27$) and increasing amounts of Cs+ (n), showing that the perovskite is photo-stable for CsI deposition rates > 0.3 Å/s.

In order to confirm that perovskite films obtained with CsI deposition rates > 0.3 Å/s are photostable, we have fit the PL spectrum in Figure S1c. The generalized Planck's law describes the radiation of a non-black body under a potential difference (quasi Fermi-level splitting, $\Delta\mu$) and reads in the Wien-approximation

$$I_{PL}(E) = \frac{2\pi}{h^3c^2}\frac{E^2\alpha(E)}{exp\left(\frac{E-\Delta\mu}{kT}\right)}$$

where E is the photon's energy, h is Planck's constant, c is the speed of light, $\alpha(E)$ is the absorptance of the semiconductor and kT is the thermal energy. From this, one can see that the slope of the PL is determined by the term $exp\left(-\frac{E}{kT}\right)$ in the low-wavelength region while it is governed by the decrease of absorptance below the bandgap in the high-wavelength region. Therefore, a PL spectrum is typically not symmetric. To show that there are no extra contributions of a low-energy phase we employed equation (1) to fit the PL spectrum of Fig. S1c using the sensitive EQE spectrum of a perovskite solar cell with equivalent composition as the absorptance.

To not be limited by the measurement noise starting at 750 nm, we extended the Urbach slope of the EQE down to 900 nm. The resulting theoretical spectrum assuming a temperature of 300 K is essentially identical to the measured PL. The small red-shift of 5 nm is likely due to a small discrepancy in the wavelength-calibration of the two measurement setups or to batch-to-batch variations in the perovskite deposition. Importantly, the quasi Fermi-level splitting does not influence the shape of the spectrum but just its intensity. We can hence conclude that we cannot see any additional phase from the PL spectra for perovskites obtained with CsI deposition rate > 0.3 Å/s.

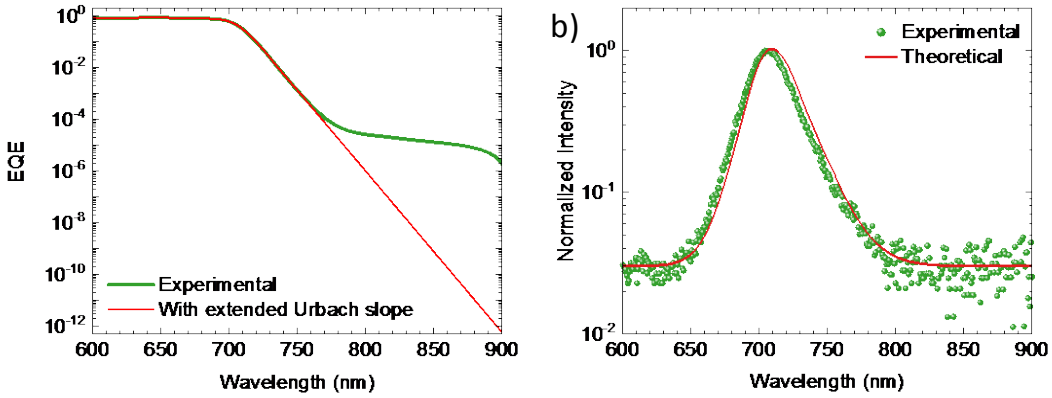

Figure S2. (a) EQE spectrum for a perovskite with bandgap of approximately 1.75 eV (Br^- content, x = 0.27) with and without the extended Urbach slope below the noise level. (b) Experimental and theoretical photoluminescence spectra for the same material, where the theoretical one is calculated using the EQE response with extended Urbach slope in (a) as the absorptance.

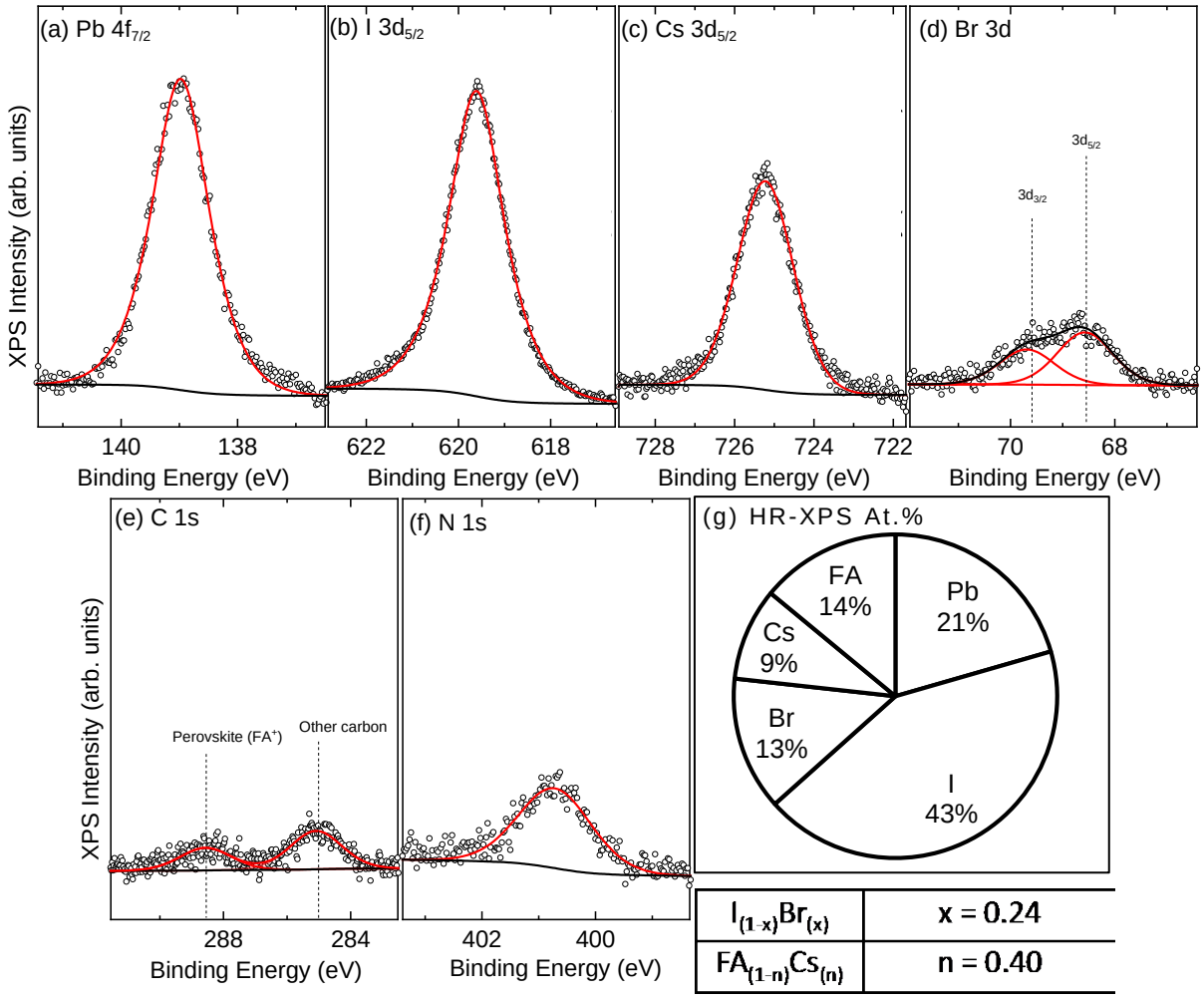

Figure S3. Top surface chemical composition. High resolution XPS spectra (Al−Kα = 1486.6 eV) of the perovskite film corresponding to core levels of (a) Pb-$4f_{7/2}$, (b) I-$3d_{5/2}$, (c) Cs-$3d_{5/2}$, (d) Br-3d, (e) C1s, (f) N-1s, and (g) atomic percentages (At.%) of the elements after normalization with corresponding elemental and spin-orbital splitting atomic sensitivity factors.

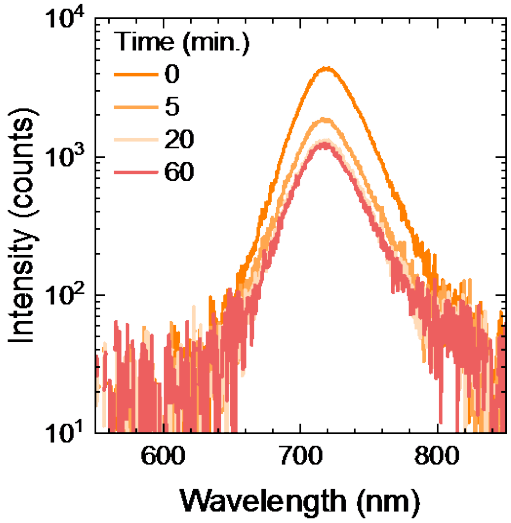

Figure S4. PL spectra recorded over time showing an initial decrease of the intensity which is found stable after 15-20 minutes of continuous irradiation.

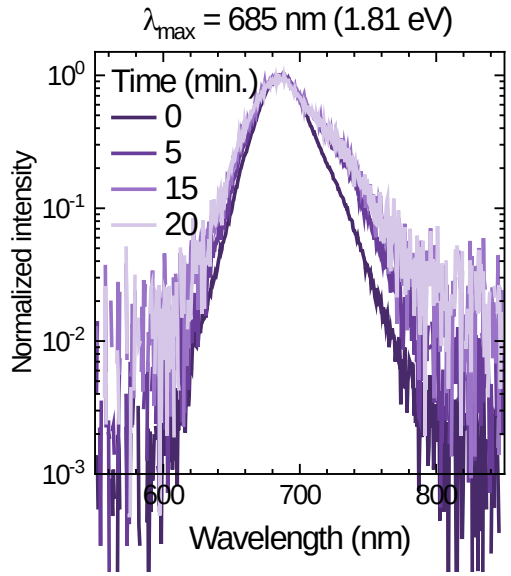

Figure S5. PL spectra recorded over time for a perovskite film of the type $FA_{0.5}Cs_{0.5}Pb(I_{1-x}Br_x)_3$ with bromide content $x = 0.4$.

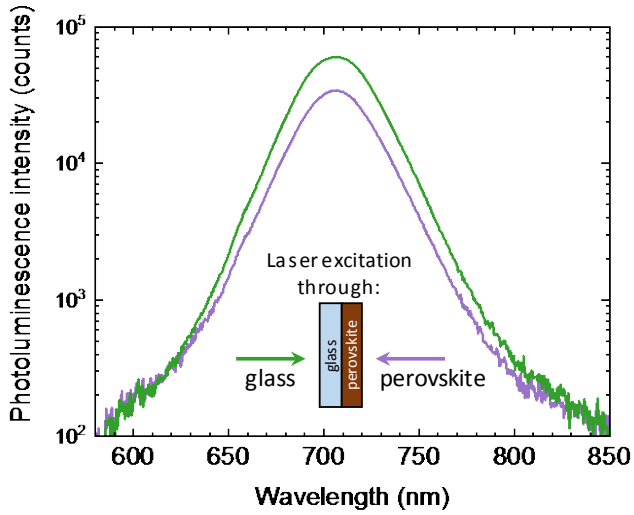

Figure S6. PL spectra for a perovskite with bandgap of 1.75 eV (Br^- content, x = 0.27) recorded by illuminating the sample through the glass substrate and through the perovskite surface.

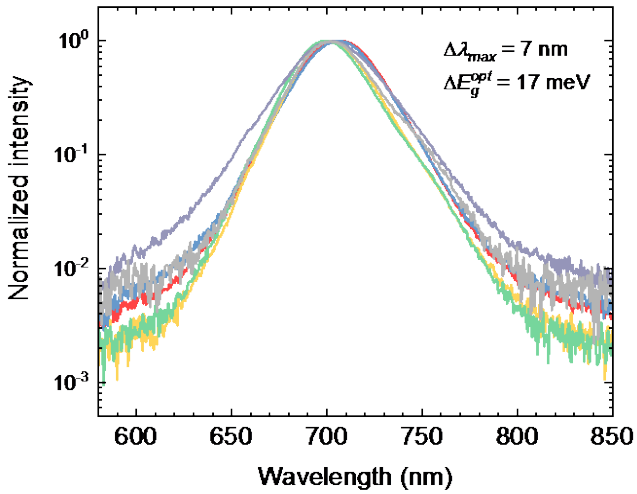

Figure S7. PL spectra for perovskite films with bandgap of 1.75 eV (Br^- content, x = 0.27) obtained from several consecutive deposition processes. The variation of the wavelength at maximum intensity (λ_{max}) is of 7 nm, corresponding to a bandgap fluctuation of only 17 meV.

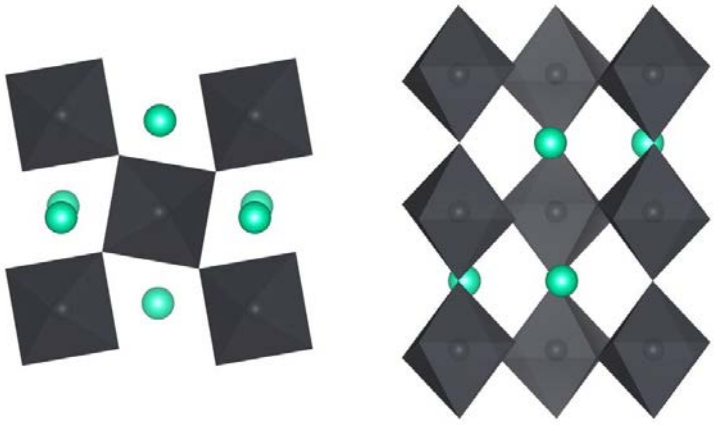

Figure S8. $CsPbBr_3$ crystal structure (Pnma space group) viewed along the b-axis (left) and c-axis (right). Green balls represent Cs^+ cations and grey octahedra represent $PbBr_6$ units.

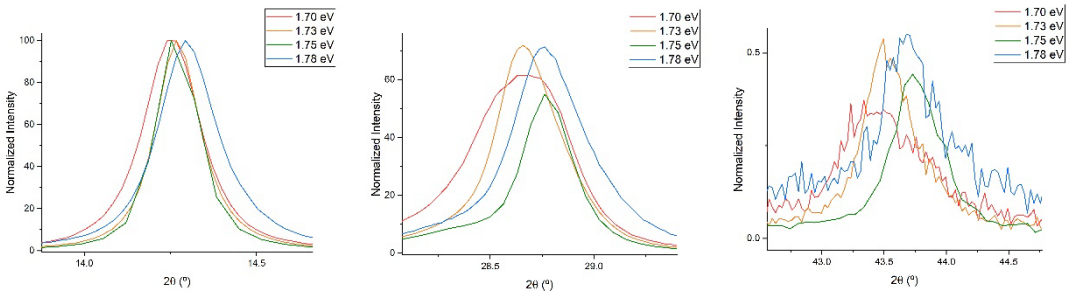

Figure S9. "Zoomed" view in some of the main XRD peaks. Samples corresponding to higher-bandgap compositions show diffraction peaks shifted to higher angles (i.e., smaller interatomic distances) as expected from the replacement of the bigger anion I^- with the smaller one Br^-. Note that unit cell volumes presented in Figure 2 are not simply derived from the direct observation of these signals but from whole-pattern deconvolution through Le Bail method, which yields a much more accurate result.

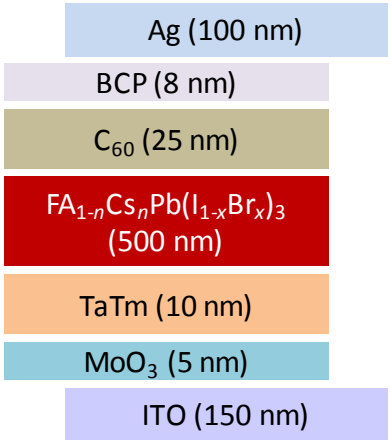

Figure S10. Schematics of the device layout used in this work.

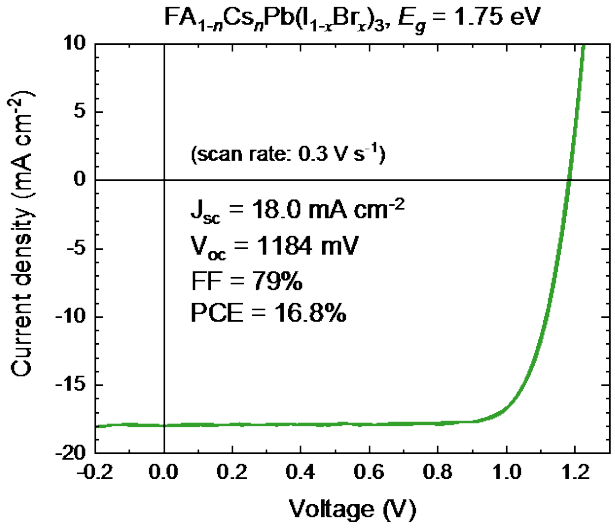

Figure S11. J-V curves under simulated solar illumination recorded in forward (from short to open circuit) and reverse (from open to short circuit) bias for the best solar cells using a 1.75 eV bandgap perovskite.

Calculation of the bandgap, Urbach energy and the radiative limit of the V_{oc} from the sensitive EQE measurement

The bandgap of an ideal semiconductor is defined as the energy where the absorption of light changes from 0 suddenly to 1. A real semiconductor has however not a sharp absorption onset but the absorption coefficient decays typically exponentially below the bandgap,

$$\alpha(E) = \alpha_0 \, exp\left(\frac{E}{E_U}\right), for \; E < E_g. \quad (1)$$

The slope of this decay is called the Urbach energy, E_U, and indicates the structural and thermic disorder in the absorber.[2,3] Here, we assumed that the EQE is proportional to the absorption coefficient and obtained E_U from a fit of the exponential decay of the EQE.

Furthermore, one can find an effective bandgap by looking at the derivative of the EQE. For the ideal semiconductor as in the Shockler-Queisser theory (SQ), this should be just a Dirac delta function at the bandgap, i.e. an infinitely high and infinitely narrow peak at the bandgap. Following Rau et al.,[4] $\frac{dEQE}{dE}$ can be interpreted as a distribution of SQ-bandgaps for a real semiconductor. It often looks similar to a Gaussian peak, so we extract the bandgap as the central energy of a Gaussian fit.

The radiative limit of the V_{oc} can be calculated with the measured J_{sc} and with the radiative limit of the dark saturation current, $J_{0,rad}$:[5]

$$V_{OC,rad} = kT\,. \tag{2}$$

This value includes the voltage losses because of difference between the measured J_{SC} and the theoretical possible value in the SQ theory as well as the radiative losses originating from the finite absorption tail.[4] To calculate the latter (corresponding to $J_{0,rad}$), we can use again the absorption tail of the EQE as a product with the black-body radiation at 300 K to calculate the luminescence spectrum at equilibrium (reciprocity relation) and integrate this:

$$J_{0,rad} = \int EQE(E)\varphi_{BB}(E, 300\ K)dE. \tag{3}$$

In the SQ theory $J_{0,rad}$ is calculated by replacing the EQE spectrum with an step-function which yields lower values for $J_{0,rad}$ and thus a higher Voc.

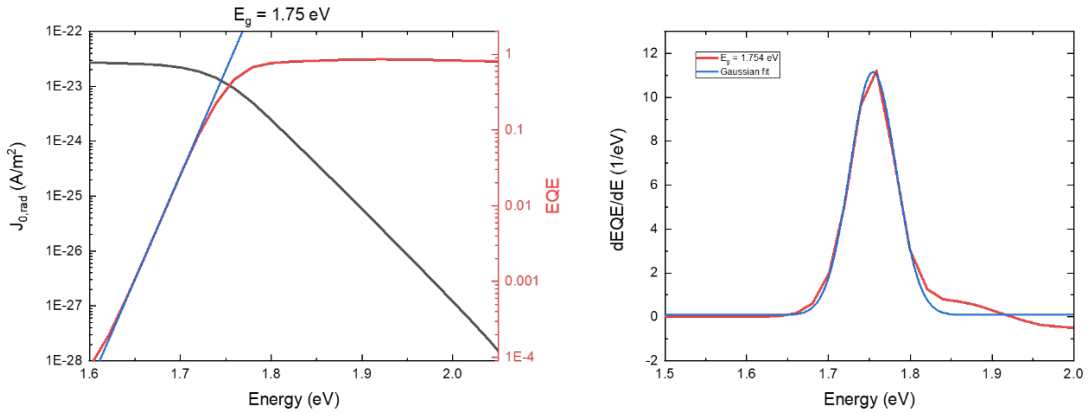

Figure S12. a) External quantum efficiency (EQE) spectrum (red) as in Fig. 4a for the perovskite with bandgap 1.75 eV with fit of the Urbach tail (blue) and integrated dark saturation current

(black). b) Derivative of the EQE spectrum (red) with Gaussian fit (blue) to determine the bandgap.

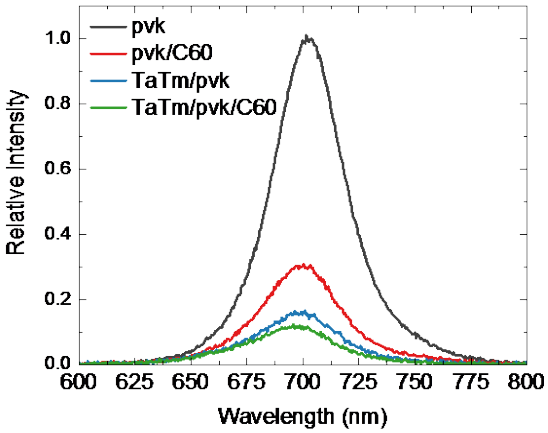

Sample	Relative PLQY	QFLS difference (eV)
pvk	1	0
pvk/C60	0.332	-0.028
TaTm/pvk	0.182	-0.044
TaTm/pvk/C60	0.138	-0.051

Figure S13. PL spectra of a perovskite film on glass, with and without the charge transport layers used in the solar cells. The relative PLQY for each variation is calculated by integration of the spectra and normalized to the one of the bare perovskite (PLQY =1). The corresponding QFLS difference calculated for each layout is also reported.

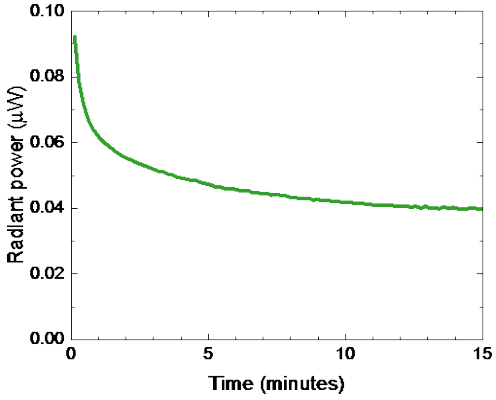

Figure S14. Time-dependent electroluminescence intensity for a perovskite solar cell in forward bias with a current density equivalent to its short circuit current.

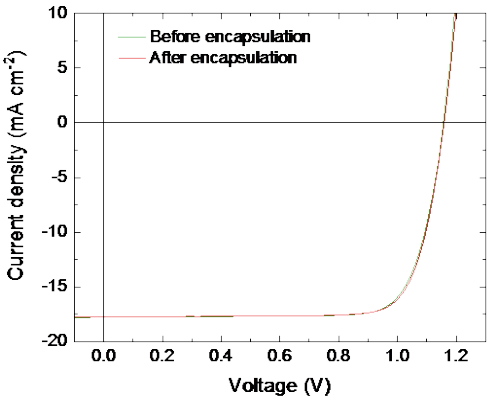

Figure S15. J-V curves for a wide-bandgap $FA_{0.65}Cs_{0.35}Pb(I_{0.73}Br_{0.27})_3$ perovskites solar cell with E_g = 1.75 eV before and after encapsulation.

References

(1) Scofield, J. H. Hartree-Slater Subshell Photoionization Cross-Sections at 1254 and 1487 EV. *J. Electron Spectros. Relat. Phenomena* **1976**, *8* (2), 129–137. https://doi.org/10.1016/0368-2048(76)80015-1.

(2) Urbach, F. The Long-Wavelength Edge of Photographic Sensitivity and of the Electronic Absorption of Solids. *Phys. Rev.* **1953**, *92* (5), 1324–1324. https://doi.org/10.1103/PhysRev.92.1324.

(3) Cody, G. D.; Tiedje, T.; Abeles, B.; Brooks, B.; Goldstein, Y. Disorder and the Optical-Absorption Edge of Hydrogenated Amorphous Silicon. *Phys. Rev. Lett.* **1981**, *47* (20), 1480–1483. https://doi.org/10.1103/PhysRevLett.47.1480.

(4) Rau, U.; Blank, B.; Müller, T. C. M.; Kirchartz, T. Efficiency Potential of Photovoltaic Materials and Devices Unveiled by Detailed-Balance Analysis. *Phys. Rev. Appl.* **2017**, *7* (4), 044016. https://doi.org/10.1103/PhysRevApplied.7.044016.

(5) Rau, U. Reciprocity Relation between Photovoltaic Quantum Efficiency and Electroluminescent Emission of Solar Cells. *Phys. Rev. B* **2007**, *76* (8), 085303. https://doi.org/10.1103/PhysRevB.76.085303.